Chinese Journal of Analytical Chemistry 51.8 (2023) 100286

Contents lists available at ScienceDirect

Chinese Journal of Analytical Chemistry

journal homepage: www.elsevier.com/locate/cjac

Recent advances in metal-organic frameworks synthesis and characterization with a focus on electrochemical determination of biological and food compounds, and investigation of their antibacterial performance

Mehdi Khalaf Mohammad MAHJOOB[a], Mahshid AKBARIZADEH[b], Paria HASHEMAN[c], Natthaporn RATTANAPAN[d], Ali MORADI-GHOLAMI[e,*], Hawraz Ibrahim M. AMIN[f], Abduladheem Turki JALIL[g], Marwan Mahmood SALEH[h,k]

[a] *College of Science, Biology Department, Wasit University Iraq, Iraq*
[b] *Department of Environmental Health Engineering, School of Public Health, Iran University of Medical Sciences, Tehran, Iran*
[c] *Chemistry Research Center, Science and Research Branch, Islamic Azad University, Tehran, Iran*
[d] *Faculty of Agricultural Technology, Phuket Rajabhat University, Muang, Phuket 83000, Thailand*
[e] *Azad University of Masan, Masan, Iran*
[f] *Department of Medical Biochemical Analysis, Cihan University-Erbil, Erbil, Iraq*
[g] *Department of Medical Laboratories Techniques, Al-Mustaqbal University College, Babylon, Hilla 51001, Iraq*
[h] *Department of Biophysics, College of Applied Sciences, University of Anbar, Iraq*
[k] *Medical Laboratory Technology Department, College of Medical Technology, The Islamic University, Najaf, Iraq*

A R T I C L E I N F O

Keywords:
Metal organic frameworks
Nanostructures
Electrochemical sensors
Modified electrode
Antibacterial activity

A B S T R A C T

Metal-organic frameworks (MOFs) are hybrid materials composed of both organic and inorganic elements. MOF materials, because of their unique structures and properties, such as controllable pore size, large surface area, excellent catalytic activity, and high density of active sites, are applied in electrochemical sensors systems for the sensitive, quick, and low-cost detection of multiple analytes. MOFs, with their high specific surface area, controllable shape, and adjustable pore volume, will provide strong interaction with compounds via abundant functional groups, leading to increased selectivity for electrochemical determination of a wide range of compounds. In this review, the structure, synthesis methods, characterization, and the applications of MOFs in recent years as sensing material in fabricating sensors for detecting drugs, pesticides, heavy metals, food additives, and other contaminants are summarized, compared, and discussed. Also, MOFs were used in numerous antibacterial application areas due to their long-term release pore volume, capability, and stretch ability when integrated with a wide range of compounds and/or substances (including nanostructures, phytochemicals, antibiotics, and polymers). This review also provides a comprehensive overview of the antibacterial uses of MOFs and one's composite materials, with a focus on the different kinds of MOF nanocomposite and their antibacterial influence in various uses.

1. Introduction

Metal-organic frameworks (MOFs) are crystalline compounds formed of metal ions and organic ligands that assemble into highly ordered structures [1]. "MOFs" is an abbreviated form for MOFs that is a common term for the class of compounds. Tomic's first publication on porous materials and MOFs in 1965 piqued the interest of scientists at the time [2,3]. The significance of materials is determined by the role they play in daily life and their impact on the future of human technology [4]. Numerous MOFs are classified based on where they were discovered, such as UiO, MIL, HKUST, and LIC [5]. MOFs are at the core of contemporary coordination science and chemistry, as evidenced by the spectacular (and always growing) amount of literature showing up in the published studies in the last two decades (Fig. 1), which is expected to reach 40 thousand papers by 2020. Several recent review papers and books, for example, clearly demonstrate the enormous potential of this group of materials [6]. The following five developments can be attributed to the nearly unprecedented increase in MOF investi-

* Corresponding author.
E-mail address: a.moradi400@yahoo.com (A. MORADI-GHOLAMI).

https://doi.org/10.1016/j.cjac.2023.100286
Received 25 March 2023; Received in revised form 23 May 2023; Accepted 25 May 2023
Available online 27 May 2023

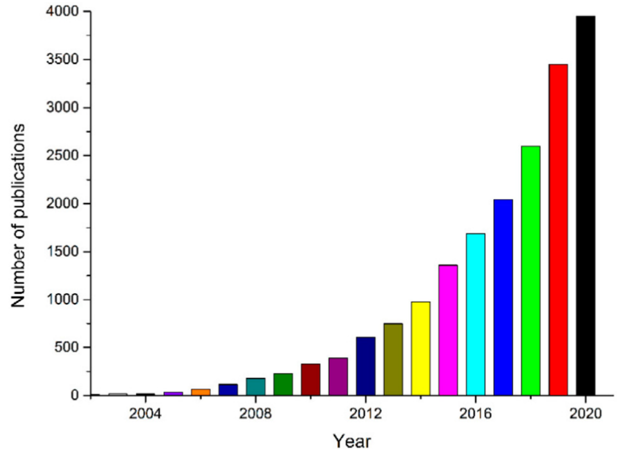

Fig. 1. The amount of literature with the words "MOF" in their titles or keywords from 2002 to 2020. Data reproduced from [6].

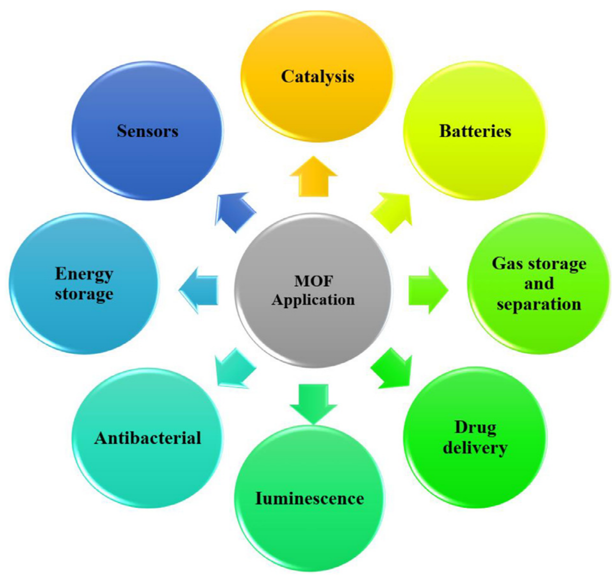

Scheme 1. Application of MOFs in different fields.

gation: (1) integrative development of MOF studies with its neighboring fields, (2) framework determination, especially through X-ray crystallography, and advancement of hard- and applications for assessing adsorptive characteristics, (3) mental development of organic synthesis appropriate to ligand preparation and post-synthetic modification, (4) the always advances in uses and (5) improvements in cluster chemical properties [7].

Numerous areas of science, including physics, math [8], chemistry [9,10] and medicine, have advanced significantly in recent years [11–26]. Nanomaterials play an important role in many of these sciences [27–37]. nanostructures have been widely used in catalysis [38–40], batteries [41], photocatalyst [42,43], biological [44–48], gas storage and separation [49], drug delivery [50–52], luminescence [53], supercapacitors [54], energy storage [55], antibacterial [56], removal [24,57,58], sensor [59], diagnosis [60–63] and so on [64–66] (Scheme 1). MOFs because of their large surface area, the huge number of available active metal sites, steady framework, nontoxic existence, and porous framework, MOFs have emerged as a major generation substance for many applications [67] such as essential electrochemical sensors [68]. Nevertheless, the isolator properties of organic linkers and the d-orbital involvement of coordination ions among both metal ions and organic linkers prevent electrons from delocalizing successfully across the entire structure. As a result, MOFs have low conductivity and poor stability, limiting their use in these fields. To address these issues, a feasible plan is to develop composite materials that incorporate the benefits of every element [69]. The use of MOF-based nanocomposite in conjunction with some other composite materials can enhance electrical properties and stability [70].

Based on the types of output signals that sensors produce, they can be broadly categorized. Between them, electrochemical sensors are the most distinctive and well-liked technique that allows for the analysis and quantification of the target molecules while demonstrating considerable reproducibility and reduced detection limits and good dynamic ranges [71,72]. Furthermore, the benefits of *in-situ* sensing, immediate reaction, and cost effectiveness allow it to be applied to the development of real-time diagnoses Point-of-Care (POC) miniaturized systems even for whole cells without endangering people. To assess a sensor's performance, it is essential to consider analytical parameters like sensitivity, dynamic detection range, response time, selectivity, limit of detection (LOD), precision and diagnostic accuracy, stability, and reproducibility [73]. Electro-analytical processes are extraordinarily regarded for analyte detecting because of their corresponding instrumental simplistic analysis, accessibility, sensitivity, flexibility, reliability, and stability as evidenced by research findings [1]. For the analysis of electroactive materials such as food, pharmaceutical, and environmental samples, electrochemical techniques work well. Because of their high sensitivity and selectivity, electrochemical sensors are ideal for the detection of compounds. In summary, when using conventional electrodes, no peak is observed at lower amounts of the analyte. These sensors have numerous limitations that create them less appealing for market availability. These constraints drew researchers' attention to the possibility of modifying the surface of the electrodes. Modified electrodes with appropriate mediators play a critical role in achieving this sensitivity and selectivity [74]. Furthermore, modified electrodes can be used to investigate a variety of materials and provide numerous benefits in the development and design of electrochemical electrodes [75].

According to research, chemically modified electrodes (CME) have one conductive surface that has been modified with monolayers, electroactive thin films, or thick surface coating. The enhanced electron transfer kinetics can be achieved by modifying the conductive surface [76]. Covalent bonding, irreversible absorption, electro-polymerization, self-assembled layers, and other such modifications are examples. It is worth noting that surface modifications play a catalytic role [77]. Furthermore, the sensitivity of measurements in electro-analytical applications might be determined by minor changes in surface characteristics. Typically, modified surfaces result in the following scenarios:

(1) Trying to transfer the modifier's physicochemical properties to the sensor.
(2) Increased electro-catalytic activity due to the use of materials with greater surface areas, would enable a higher level of sensitivity.
(3) Because of the adsorbed functional groups and doping, the selectivity is more toward the substance.
(4) In a wide range of compounds, rapid diffusion kinetics exist.
(5) Analyte accumulation and extraction at the sensor [78].

Nanomaterials were crucial in the modification of sensors, which significantly improved the potential and sensitivity of electrochemical electrodes. The appropriate modification of sensors enabled the rapid detection of electroactive contaminants at extremely low concentrations and provided a viable determination procedure available for signal fluctuation and over voltage. Nanostructures have recently emerged as being the most suitable candidates in the research area of electrode modification, owing to their increased surface area and high catalytic characteristics, and have had a significant impact on the detection procedures for numerous electroactive compounds [79].

The bacterial disease, which is still one of the going to lead causes of illness and death, is a major public health concern around the world [80,81]. Although synthetic antiseptics, antibiotics, and other types of microbial biocides were discovered and developed to combat pathogens, overuse of antibiotics results in antimicrobial resistance (AMR) [45,82–85]. Multidrug-resistant (MDR) microbes have emerged as a result of AMR's emergence and spread, posing a growing threat to international population safety. According to the latest prognostications through the World Health Organization (WHO), antibiotic-resistant microbes impact the safety of around 60 percent of the population every day around the universe, and the percentage will rise to 10,000,000 by 2050, surpassing cancer's current toll [83,86]. Various studies have recently revealed that nanostructures have excellent antimicrobial properties in the fight against bacteria. MOFs and nanocomposites derived from them have been considered potential antimicrobial components [87,88]. According to their frameworks and morphological characteristics, over 20,000 MOFs were developed to the deadline, which can be categorized as 3D hierarchical structures, 2D nanosheets, 1D nanowires, 0D nanostructures, nanotubes, and nanorods. MOFs' diverse properties make them perfect components for a wide range of antimicrobial uses [89–91].

This review focuses on MOF nanostructures and their application in electrochemical detection. First, the methods of MOF synthesis and characterization are discussed. In the following, the applications of these nanostructures for electrochemical detection of various compounds such as nitrofurazone, fentanyl, and heavy metal ions are investigated. In addition, the antibacterial properties of several MOFs and composites prepared using them were also investigated.

2. Structure of MOFs

In recent years, different sciences have made significant progress in various fields [92–116] such as nanotechnology. There are different types of nanostructures, among which we can mention nanofluids [20,117–127], nano stars [128], nano layer [129], nanoparticles [130–133], core-shell [134], nano powders [135,136], nanorods [137,138], MOFs [139], nanosheets [140], nanoplates [141], carbon nanotubes [142–145], etc. MOFs seem to be nano porous combination constituents made up of metal oxo groups linked by organic groups [146,147]. MOFs include both organic links and metal centers in their structure. Organic connections are regarded as natural SBUs (Secondary Construction Components) that behave as struts, whereas metal centers are inorganic SBUs that behave as 'joints' in MOF structures. SBUs seem to be simple geometrical organizations composed of inorganic clusters decided to join by organic material to establish a framework product that is manufactured *in situ* in the reaction under properly defined circumstances [148]. MOFs, which are formed by the coordination of a metal ion and an organic ligand, are a highly porous 3D platform that is rich in functional groups [149]. If MOFs were designed using expanded zeolite topology, their inorganic and organic structures would have larger pores and higher porosity than zeolites. High porosity size is caused by the enlarged size of inorganic SBUs and the network dimensions caused by massive metal clusters. Furthermore, due to rising porous structure and extremely long organic ligands benefiting high porosity diameter, the distance of the link among synthetic SBU is increased. MOFs as molecular building blocks are created using various metal centers and linkers, resulting in appropriate flexibility for adjusting physical and chemical properties [150–153]. The scheme of MOFs is depicted in Scheme 2.

3. Properties of MOFs

By blending organic and inorganic elements, MOFs have demonstrated unique properties such as remarkably large surface area (up to 6000 m^2/g), controllable structure, consistent but controllable porosities (0.5 to 2 nm), ultra-high pore volume (around 90 percent free volume), bare and completely exposed active sites, and plentiful combinations (Scheme 3) [154–157]. Because of their porous structure and large specific surface area, MOFs were also identified as a superior framework for immobilizing chemical catalysts on conductive precursors. Furthermore, these materials can be modified to have high selectivity towards a specific chemical response [2,158,159].

MOFs' distinct properties drive their rapid development in a variety of scientific fields, including sensors. Nevertheless, a few issues, particularly low electroactivity, have hampered their widespread application. Because most MOFs' electrochemical-catalytic ability is suboptimal, obtaining ideas to enhance their electrocatalytic activity is a critical issue for furthering their applications in the electrochemical research area [160–162]. In recent times, an increasing number of studies have indicated the ability of MOFs for electrochemical sensors. MOF/metal nanoparticle composites, for example, have been investigated for electrochemical sensing to improve the obvious problem of MOF [163–165]. As a result, suitable MOF-based materials with high conductivity and numerous catalytic sites must be established for the electrochemical research approach.

4. Synthesis of MOF

MOF synthesis employs experimental conditions that influence the porous structure, morphological characteristics, and crystalline nature. As a result, it is essential to select a synthesis method that controls the physiochemical properties of the procured ingredients. Furthermore, especially in large-scale synthesis, it is critical to consider the economic and environmental aspects. Depending on the resulting frameworks and properties, a variety of synthetic methods can be used to generate MOFs. These methods include slow diffusion, reflux, electrochemical, hydrothermal, sonochemical, coprecipitation, and thermal decomposition techniques.

4.1. Slow diffusion method

The slow diffusion method is liquid-liquid diffusion, in which two layers of liquids refer to this process to concentration differences, one of which is the precipitant soluble and the other of which encircles the product. A third solvent layer separated the two layers [166,167]. The gradual diffusion of the precipitating liquid into the dividing layer causes nucleation and growth at the interface. The reactants in two vials of varying sizes are progressively dispersed in the second method by diving them with physical barriers. The diffusion method allows for the formation of single crystals suitable for the X-ray diffraction (XRD) technique as a replace for non- or poly-crystalline ingredients, mainly when the products are dissolvable [168,169].

Singha et al. successfully synthesized a new Cd-based MOF using the slow diffusion technique at ambient temperature to avoid energy consumption and pressure dangers. The MOF has potential applications in gas adsorption, separation, and catalysis due to its porous structure and high surface area. The MOF was characterized using single crystal structural characterization, powder XRD, infrared spectroscopy, and thermogravimetric analysis (TGA). The results showed that the MOF has a monoclinic structure system with a P21/c space group and can be used for various applications. Further studies can optimize the synthesis conditions for improved performance [170].

Shi et al. prepared an innovate sensitizing decatungstate-based MOF. The interaction of $[(n\text{-}C_4H_9)_4N]_4[W_{10}O_{32}]$, 3-amino-4,4′-bipyridine (NPY) and $Cu(ClO_4)_2{\cdot}6H_2O$ by a diffusion method led to a novel 3D decatungstate-based MOF ($[Cu(NPY)_2(DMF)]_2(W_{10}O_{32})){\cdot}DMF{\cdot}3CH_3CN$ (also known as DT–NPY) with 1D hydrophilic/hydrophobic channels. Elements studies, Infrared spectrum, UV–Vis spectrum, single-crystal XRD, and XRD were used to study the structural of this compound. Under mild reaction conditions, DT–NPY development and rapid photocatalytic performance for oxidation of cyclohexane to cyclohexanol and cyclohexanone by oxygen molecules. The photocatalyst DT–large NPY's catalytic performance, stability, and reusability illustrate the excellence of the decatungstate ingrained MOF over homogeneous systems and other heterogenization techniques [171].

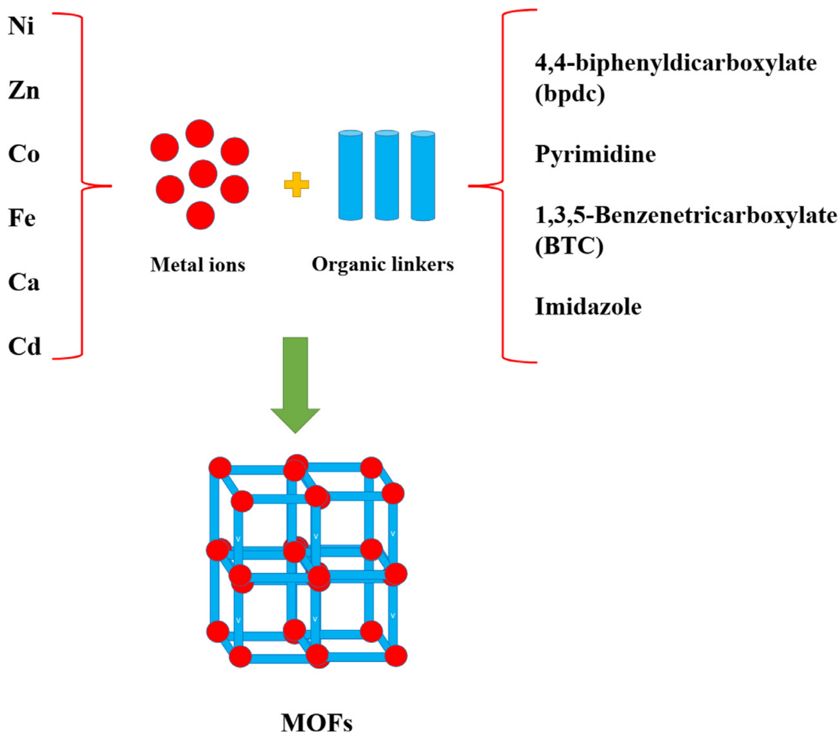

Scheme 2. Metal ions and linkers are used to synthesize MOFs in this diagram.

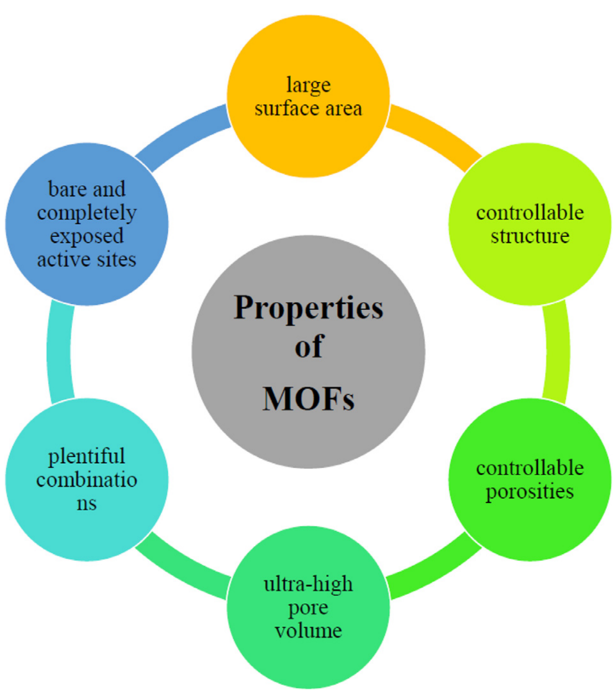

Scheme 3. Properties of MOFs.

4.2. Reflux method

The reflux method has many benefits, such as simple synthesis, environmental friendliness, controllability of surface morphology through straightforward reaction conditions, and lower cost. Because porous surfaces of nanostructures provide simple routes for ionic species trying to move from either the electrolyte/electrode interface, they enhance electrochemical properties. Furthermore, because the reflux approach is based on a liquid solution, a solid-state interaction is not feasible [172].

Patel et al. synthesized two mixed ligand MOFs, $[[Zn_2(5NO_2\text{-}IP)_2(L)_2](H_2O)]_n$ (ADES-1) and $[[Cd_2(5NO_2\text{-}IP)_2(L)_2(H_2O)_4](L)(H_2O)(CH_3OH)_6]_n$ (ADES-2) (where $5NO_2$-IP=5 nitroisophthalate and L=(*E*)-*N′*-(pyridin-3-ylmethylene)nicotinohydrazide), via various analytical approach. ADES-1 with bulk crystalline phase was created using a traditional reflux procedure. Numerous analytical techniques, such as SXRD analysis, were used to characterize both MOFs. All these MOFs use the same two-dimensional topology of the network, according to SXRD observation [173].

Siva et al. synthesized a new Mn(II) containing guanidinium-MOF using a reflux reaction strategy. The MOF was characterized using single crystal XRD, DT-TGA analysis, UV–visible spectroscopy, and Z-Scan. The MOF has a monoclinic crystalline phase with space group P21/c and strong MOFs formed by Mn–Cl bonds. The MOF has potential applications in gas adsorption, separation, and catalysis due to its porous structure and high surface area. Further studies can optimize the synthesis conditions for improved performance [174].

Dhivya et al. prepared a titanium-based hetero MOF. For this purpose, titanium-based MOFs NH_2_MIL-125 and NTU-9 were integrated to make a hetero MOF NTU-9/NH_2_MIL-125 (HMF) via refluxing method. It was characterized by XRD, TGA, FE-SEM, FT-IR, XPS, UV–vis (DRS) and PL, etc. XRD analysis appears to confirm the as-synthesized MOFs' framework structure and suggests the crystallinity and framework existence of all derived MOFs. HMF's thermal properties are enhanced to 520 °C when compared to NTU-9, and the BET surface area of NTU-9, NH_2_MIL-125, and HMF was determined to be 986, 1267, and 550 m^2/g, respectively, suggesting their micro-porous essence [175].

4.3. Electrochemical method

MOF electrochemical formation can be performed at room temperature and pressure, attempting to avoid the huge amount of energy and risks associated with a high-temperature and high-pressure process [176]. Furthermore, in the metal electrochemical fabrication of MOFs, the metal component is exposed to anodic oxidation in the presence of an applied electric current, resulting in a fast and cost-effective synthesis. The above strategy also has several benefits, including excellent yield, reduced energy consumption, simple operation, environmentally friendly nature, and the absence of the need for specialized tools.

Electrochemical characteristics including supporting electrolyte and applied voltage have been shown to play a significant role in adjusting the morphological characteristics (size, structure, and distribution of particles) and produce of the response [177,178]. But besides the appealing characteristics of this technique, the electrochemical reaction-produced MOFs also are relatively low in comparison to samples prepared through other processes, and systematic research on the impact of electrochemical factors on reaction is still required.

Asghar et al. synthesized Mn-DABDC and Mn-BDC MOFs using both electrochemical and solvothermal methods. They found that the most important factors influencing crystal formation were electrolyte quantity, current density, and response time. The optimum electrochemical conditions resulted in a shorter response time and lower fabrication costs compared to traditional solvothermal and hydrothermal techniques. The electrochemical method also reused nitrate counterions and used atmospheric temperature, making it a more cost-effective approach for designing and formulating advanced products with the potential for higher yield [179].

4.4. Hydrothermal method

The hydrothermal techniques were used to create a variety of MOFs with various sizes, morphologies, and lattice parameters. But even though a large number of MOFs have been revealed to date, numerous problems remain to be addressed, including surface charge, size, stability, toxic effects, and shape [180]. The above factors are not distinct and interact with one another. In general, hydrothermal synthesis of MOFs includes combining ionic species substances and organic ligands in a solute and having to hold the combination at extreme temps (greater than 99 °C) for long periods. MOF production involves some levels, as illustrated below [181]:

Reactant ⟶ Reactant mixture ⟶ Nucleation ⟶ Crystal growth

MOFs are produced at high temperatures in order to produce a good production of crystallites in a reasonable amount. The chemical composition of the reagents, pH, and temperature are the parameters in the fabrication. To achieve a nano-sized substance, surfactants or compound frameworks are typically used in the fabrication way [182].

Liu et al. used hydrofluoric acid pre-treatment and hydrothermal *in situ* growth techniques to fabricate a new novel Mg-MOF-74/MgF_2 compound covering. Using traditional biocompatible MOF material made of 2,5-dihydroxyterephthalic acid and Mg^{2+}, Mg-MOF-74 was produced. Mg-MOF-74/MgF_2 was synthesized using 2,5-dihydroxyterephthalic acid (0.8 mmoL) and magnesium nitrate hyxahydrate (2.5 mmoL) as a starting material [183]. Fig. 2 depicts a schematic representation of the manufacturing system for Mg-MOF-74/MgF_2 compound covering.

Cheng et al. used a microwave hydrothermal technique to successfully synthesize a new hybrid MOF (Cd/Zr-MOF) with Zr^{4+} and Cd^{2+} including 2 different ionic species and terephthalic acid (H_2BDC) as an organic linker. On the Cd/Zr-MOF system, the effects of the Cd/Zr molar percentage and reaction conditions have been thoroughly investigated. Zirconium 1,4-dicarboxybenzene MOF (UiO-66, i.e., $Zr_6(OH)_4(C_8H_6O_4)_6$) has a fantastic hydrothermal and chemical stability in Zr-based formwork due to its rigid face-centered cubic formation through twelve coordination. A recent study has also found that Cd(II)-based MOFs with metal ion doping via ionic interaction operate well in the selective adsorption and photodegradation of various compounds [184].

4.5. Sonochemical method

Sonochemical production seems to be a cost-effective, environmentally sustainable, and simple process that is gaining popularity in MOF fabrication due to its energy efficiency, short reaction rate, and ease of use. Ultrasonic energy (20 kHz 10 MHz) is required to cause physical or chemical improvements in compounds caused by bubbles in solvents that have gone through the cavitation technique's role in the creation, growth, and instantaneous collapse under ultrasound waves [185]. At high pressure and temperature, short-lived local hot spots (around 5000 K and 500 bar) can be created, while the chemical process is also supported by the excessed crystal nuclei developed under extreme conditions [186]. In comparison with the conventional hydrothermal and solvothermal techniques, the nucleation centers of MOFs might be produced homogeneously with a significantly reduced crystallization period using sonochemical formation; thus, sonochemistry has been commonly used during the production of MOFs over the recent century. The arrangement of MOFs is said to be controllable by adjusting ultrasonic levels of power, and the prepared nanoparticles have smaller particle sizes [187].

Yu et al. successfully synthesized Zr-based porphyrinic MOFs, MOF-525 and MOF-545, using a sonochemical method in a shorter time and with higher purity compared to traditional methods. The physicochemical characteristics of the MOF structures were investigated using XRD, SEM, N2 adsorption-desorption isotherms, UV–vis spectrometry, TGA, and an inductively coupled plasma mass spectrometer. The sonochemically produced MOF components had more defect sites and better textural characteristics than traditionally organized MOF samples, and the particle size of MOF-545 was considerably smaller. Overall, this method resulted in increased crystal pureness, decreased fabrication time, and enhanced physicochemical characteristics of the MOF structures [188].

Tanhaei et al. created 2-fold interpenetration zinc-based MOF/graphene oxide (TMU-16-NH_2/GO) nanocomposite products at ambient temperature and pressure using a simple, large-scale, and clean sonochemical methodology. The effect of graphene oxide concentrations on the structure and shape of TMU-16-NH_2/GO combination nanomaterials has been investigated. The appearance of GO alters the surface characteristics of nanomaterials, and the rod thickness of the GO-TMU-16-NH_2 reduced as the GO concentration was increased, while the bundle-like shape has become more irregular. The materials were studied by SEM, PXRD, FTIR spectroscopy, and BET. Pure MOF and nanocomposites MOF/GO components both have a porous structure with a small number of mesopores. The achieved results show that this method is appropriate for the production of some of the other MOFs/GO nanocomposites and could have a wide range of potential applications in various industries [189].

4.6. Coprecipitation method

The co-precipitation method is beneficial over other chemical and physical methods, including flexibility of reaction conditions, ease of processing, high crystallinity, and the capacity to make a product in greater volumes. Furthermore, the co-precipitation procedure can be used to create materials with narrower crystal sizes and porous structure morphologies. Nevertheless, such a strategy necessitates the use of high-quality liquids, water for washing, and also more drying conditions [172].

Zhou et al. used nanosized silica-coated zerovalent iron and MOF-5 to make preparations for new magnetic nanocomposites of type Fe@MOF-5 using a co-precipitation approach. TEM and XRD were used to examine its morphology and structure. The findings revealed that the established process used to have some benefits, including ease of material preparation, easy procedure, easiness, and low price, making Fe@MOF-5 suitable candidates for combining magnetic materials and

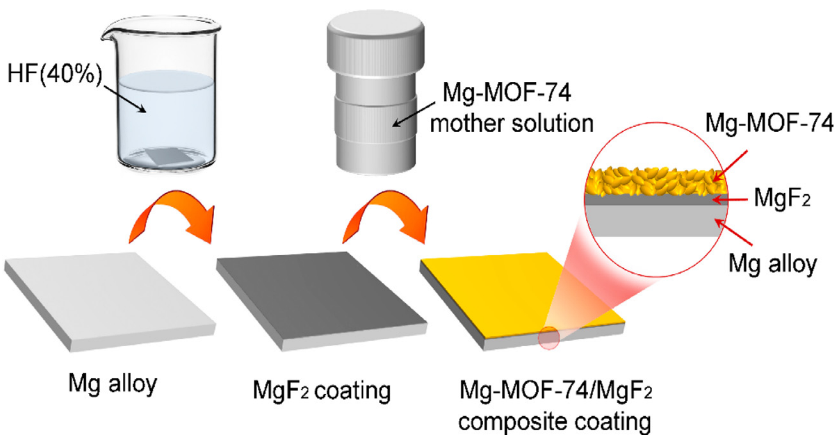

Fig. 2. The preparation of the Mg-MOF-74/MgF_2 composite coating is depicted in a schematic diagram. Data reproduced from [183].

MOFs and expanding their approval process in the analysis and environmental areas [190].

4.7. Thermal decomposition method

Recently, a new method of preparation, thermal decomposition from MOFs as precursor materials to make preparations for nano-metal oxides, has been quickly developing. Numerous investigators have used this technique to produce several more metal oxides, which have been used in a variety of fields. Metal oxides with unique surface morphology could be created by combining different types of MOFs, and these metal oxides can inhibit the agglomeration of composite materials while also lead generation nanopores, improving the contact among both nanoscale particles and metal oxides. Conventional processing conditions could resolve problems such as particle agglomeration, irregular dispersion of active ingredients, and uncontrollable nanostructure [191].

MOFs have been commonly used in the thermal treatment of corresponding porous metal oxides. The high thermal procedure, on the other hand, every time results in metal oxides with huge crystal sizes, reducing their specific surface area. Iqbal et al. synthesized a nanocomposite MOF (Fe_2Ni-MIL-88B) through the use of cluster fabrication, which was then thermally decomposed in the atmosphere to yield nanocrystals $NiFe_2O_4$ nanorods (NRs) of various sizes. The pristine MOF's stoichiometry of Fe:Ni (2:1), as well as its pore volume and crystal morphological characteristics, were maintained in the final spinel nickel ferrites. Their strategy, which eliminates the use of higher boiling point liquids and surfactants, has the potential to be advanced to achieve other spinel ferrites including $CoFe_2O_4$ and $MnFe_2O_4$ [192].

5. Characterization of MOFs

XRD patterns, FESEM, TEM images, FT-IR spectrum, and TGA analysis were used to characterize and analyze the manufactured MOF specimens.

5.1. XRD of MOFs

Alduhaish et al. described an environmentally friendly and simple photocatalytic process for the production of Zr-containing MOF-801 and a silver (Ag) NPs-based composite (Ag@MOF-801). The photocatalytic possession of the metal center (Zr) of MOF was included in this technique to develop a new generation and deposition of Ag NPs on the surface of the MOF-801 when exposed to illumination. XRD was used to confirm the important to incorporate of Ag NPs [193]. Using $AgNO_3$ as a starting material, Ag NPs were placed on MOF-801. The visible source of light and photocatalytic characteristics of the metal center (Zr) of MOF was used in this efficient and environmental strategy to enhance

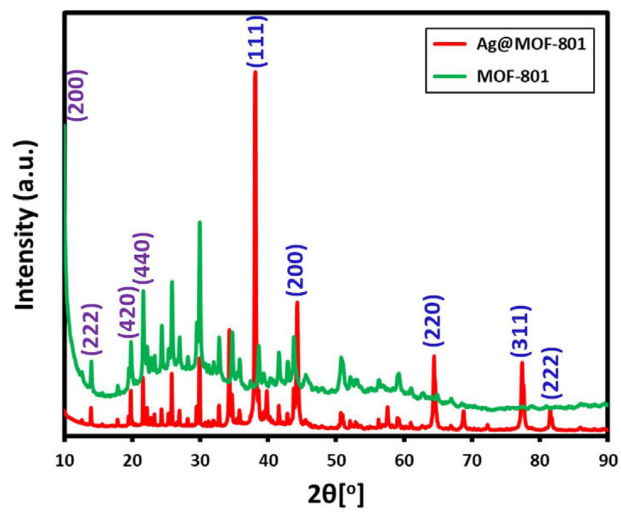

Fig. 3. XRD patterns of MOF-801 and Ag@MOF-801. Data reproduced from [194].

the successful reduction of metal precursors to create the Ag@MOF-801 combination. At first, the creation of MOF-801 was confirmed by comparing the XRD pattern of the as-prepared MOF (see Fig. 3) to previously published results. As can be seen in Fig. 3, the XRD pattern of Ag@MOF-801 contains numerous supplementary reflections in addition to the MOF-801 characteristic reflections, namely the reflections at 10°, 13.9°, 19.9°, and 21.7°, which are given to the (200), (222), (420), and (440) planes. The supplementary reflections seen at 37.5°, 44.1°, 64.3°, 79.3°, and 81.2° are the typical reflections of Ag NPs from the (111), (200), (220), (311), and (222) Miller indices. The above demonstrates that the Ag NPs on MOF-801 formed an extremely high nanocrystals, face-centered cubic (fcc) frame [194].

Gaikwad et al. presented 3 new and more effective MOFs derived from the organic ligands 1, 3, and 5-tris (1*H*-benzo[d]imidazole-2-yl) benzene (TIBM). The established TIBM crystal particles, the PXRD to prove the crystalline phase, TGA measurements to investigate the thermal stability, the BET technique for analysis of structures, and SEM were used to approximate the morphological characteristics of the nanoparticle. The performance of the TIBM-MOFs had been improved, and the components were effectively dopant with three ionic species via ionic compounds. The XRD pattern of the TIBM-MOFs matched the designed to simulate the structure of UiO-66 from the Cambridge Structural Data file (CCDC 837,796). The patterns of TIBM-Cu and TIBM-Al seem to be constant with that of the Cu-BTC and HKUST-1, respectively, whereas TIBM-Cr is comparable to MIL-101 (Fe) and Fe-BTC, verifying the suc-

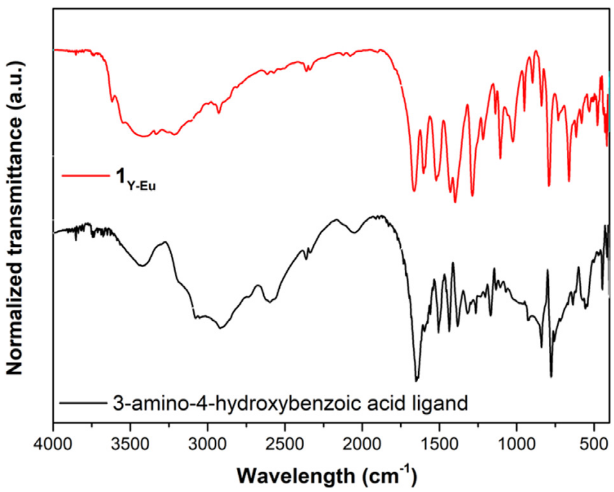

Fig. 4. A figure of the ligand and Y/Eu-MOF infrared spectra. Data reproduced from [128].

cessful formation and integrity of the crystalline lattice after coordination with TIBM. A widespread peak indicated chelation and a sharp peak at 2θ qualities of 9° and 18°, respectively, providing strong indications of the crystalline phase of the TIBM-Al Compound. The Cr-TIBM MOF showed blunt peak intensities at 2θ values of 10° and 18°–20°, a significant increase in the MOFs' crystallization level. The Cu-TIBM MOF, on the other hand, demonstrated sharp crystal peaks similar to those of the Cu-based MOFs [195].

5.2. FT-IR of MOFs

Vaidya et al. developed a method to encapsulate glucoamylase within ZIF-8 using functionalized carboxymethylcellulose (CMC) under mild aqueous conditions, resulting in a glucoamylase bio-MOF. The structural changes were investigated using FT-IR spectroscopy, which revealed successful synthesis of the bio-MOF. The MOF had a meaningful band of Zn–N at 418 cm^{-1} and diffraction peaks at 692.79, 760, 953.16, and 1306.79 cm^{-1}. CMC had diffraction patterns at 3281, 3355, 3423, and 2829 cm^{-1}, while the glucoamylase bio-MOF spectra showed the recognizable amide I band at 1668.38 cm^{-1} along with all peaks correlating to bio-MOF, confirming the effective encapsulation of glucoamylase into bio-MOFs [196].

Makuve et al. investigated a cadmium(II) MOF, $[Cd(bdc)(DMF)]_n$ (MOF1), synthesized by treating benzene-1,4-dicarboxylic acid with four equivalents of $[Cd(NO_3)_2]$. MOF1 was being used to support Pt, Ni, and Pd nanoparticles, resulting in MOF1/Pt, MOF1/Ni, and MOF1/Pd. FTIR was used to characterize these MOF-based substances. FTIR analyses (Fig. 4) were used to describe the attribute carboxylate moiety (C=O) and investigate adjustments in binding mode throughout MOF Fabrication. In MOF1, the observed C=O stretching in the linker (bdc) at 1666 cm^{-1} shifted to a reduced absorbance peak of 1652 cm^{-1}. This demonstrates the metalation procedure of bdc. MOF1, MOF1/Pt, MOF1/Ni, and MOF1/Pd FTIR spectra all have the same absorption band. The N–H stretching vibration of the amine group of the 3-amino-4-hydroxbenzoate ligand is credited to a thin peak at around 3617cm^{-1} in the FTIR spectrum of Y/Eu-MOF. The spectrum also demonstrates an extreme and broad band contributed to the free ligand's O–H bond, as well as the establishment of poor bands among 3325 and 2917 cm^{-1} corresponding to the C–H vibrations of the aromatic ring of the 3-amino-4-hydroxybenzoate linker. Peaks in the 1683–1408 cm^{-1} range are caused by asymmetric stretching vibrations of carboxylate groups and aromatic C–C and C–N bonds. The reduced range of signals, 1390–1263 cm^{-1}, can be connected to symmetric stretching vibrations of carboxylate groups. The residual peaks at low frequency resulted from ligand aromatic and carboxylate group distortions. Below 660 cm^{-1}, vibrational bands M–O, and M–N bonds are demonstrated [197].

5.3. FESEM of MOFs

Rabiee Faradonbeh et al. successfully synthesized Cu(tpa)·(DMF) (Cu terephthalic acid dimethylformamide) MOF-5 and its hybrids by hydrothermal process. SEM images of MOF-5Cu and MOF-5–Graphene hybrids (30%) were examined. The SEM results of the MOF-5 and MOF-5–Graphene hybrid 30 percent demonstrate that graphene sheets act as partitions and are placed among MOF-5Cu platelets. In the cubic crystals, the SEM of MOF-5Cu is immediately evident. Terephthalate linkers are coordinated to a CuII dimer in a bidentate connecting manner in this compound. So every CuII atom is also coordinated to a DMF molecule, resulting in a square-pyramidal coordination geometry for the CuII atoms. As a result, the CuII molecules are coordinated with the tpa linkers in the system. These layers are then bonded using weak stacking interactions comparable to MOF-5 [198].

Nguyen Thi et al. used the solvothermal process to make specimens of the bimetallic-based NH_2_MIL-125(Ti) with a Mn^+/Ti^{4+}ratio of 0.15 (Mn^+:Ni^{2+}, Co^{2+}, and Fe^{3+}). XRD, FTIR, Raman spectra, SEM, BET, and UV–Vis diffuse reflectance spectroscopy (UV–Vis DRS) were used to investigate their basic characteristics. SEM images were used to examine the surface morphologies of NH_2_MIL-125(Ti) and 15% M/Ti-MOFs (M:Ni, Co, and Fe) (Fig. 5). The obtained samples were made up of a few well-crystallized block-like molecules of various shapes, as shown in the reduced-magnification SEM images (Fig. 4). The disk-shaped molecules and narrow, in the NH_2_MIL-125(Ti) have a mean size of 0.7 m, which is comparable to the catalyst used in recent research conducted. When the transition metal ions were added to NH_2_MIL-125(Ti), the grain size rose exponentially [199].

Utilize zinc acetate dehydrate and benzene-1,4-dicarboxylate (BDC) at various temperatures, 90 °C, and ambient temperature either with or without tri-ethylamine (TEA) as a capping agent, Mehmandoust et al. prepared the MOF-5 by solvent and solvothermal techniques through the self-assembly of main building blocks. SEM was used to characterize the samples. SEM images revealed that the frameworks are cube-shaped in structure with a rough surface. The appearance of tri-ethylamine in MOF-5(I) and MOF-5(II) precludes the crystallization process, resulting in smaller particle sizes. Because of the growing phenomenon in MOF-5(III) and MOF-5(IV), rising temperatures led to an increase in particle size (IV). MOFs with cubic structure have an average size of 250 nm for MOF-5 (I), 100 nm for MOF-5(II), 800 nm for MOF-5(III), and 600 nm for MOF-5(IV) based on SEM images. These findings support the hypothesis that the process conditions alter the size of MOF-5 and that the use of a capping agent induces MOF-5 to be created in a smaller size using the solution method [200].

5.4. Thermogravimetric analysis (TGA) of MOFs

Shaik et al. demonstrated the prepared methods and applications of catalysis of Zr-fumarate-MOF (also known as MOF-801). A wide range of characterization methods, such as XRD, SEM, EDX, FT-IR, BET, and TGA analyses, have been used to confirm the creation of MOF-801 and its structural stability. MOF-801 was exposed to TGA analysis (Fig. 6) to determine its thermal stability that confirmed losing weight up to 500 °C in 3 steps. The sample lost 25% of its weight at temperatures around 125 °C, which can be attributable to the sample losing humidity. Following that, at approximately 125 and 350 °C, some other 25% to 30% losing weight happened caused by the evaporation of guest molecules, including such solutes, from the sample's cavities. The sample began to disintegrate after continued heating above 350 °C, and it was entirely broken down at 500 °C involving the breakdown of the carboxy-

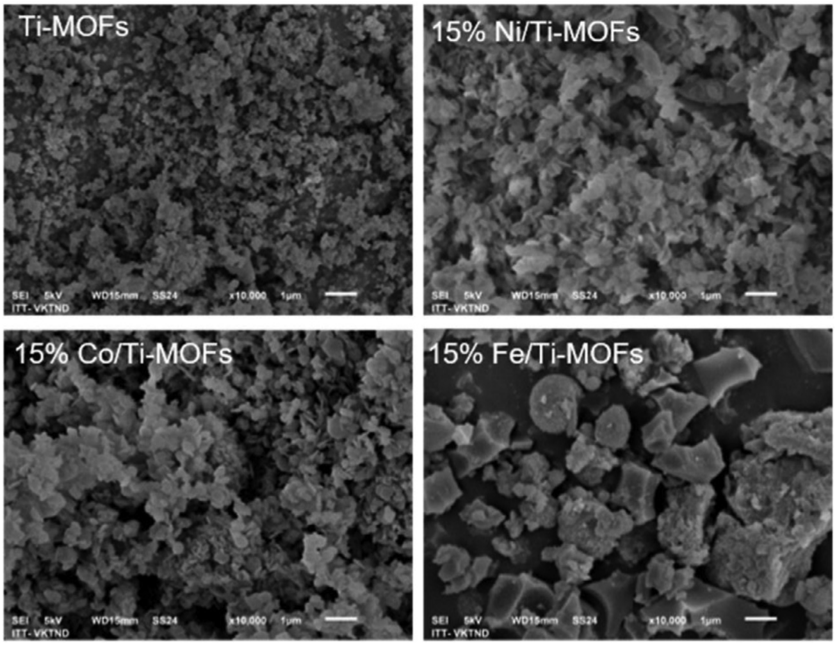

Fig. 5. SEM image of NH_2_MIL-125(Ti) and 15% M/Ti-MOFs (M:Ni, Co, Fe). Data reproduced from [199].

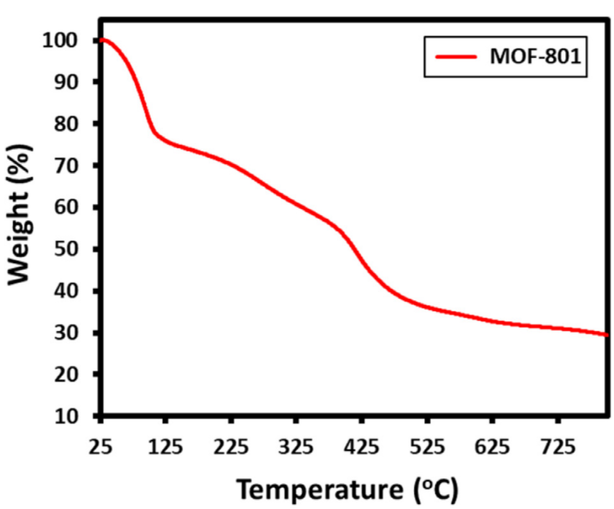

Fig. 6. TGA analysis of MOF-801. Data reproduced from [132].

late group network; this suggests the sample's good thermal stability [201].

Mohan Reddy et al. developed 3 nanodiscs ZnO@MOFs, ZnO@ZIF-8 (1), ZnO@INA (2), and ZnO@NA (3), using the structural support blocks isotonic acid, nicotinic acid, and 2-methylimidazole. FTIR spectroscopy, PXRD spectra, SEM analysis, BET analysis, and differential thermal analysis (DTA) are used to characterize these composite materials. According to TGA tests, these MOFs are stable at temperatures between 400 and 450 °C. The specific surface areas of ZnO@INA, ZnO@NA, and ZnO@ZIF-8, are determined using N_2 adsorption–desorption isotherms. BJH model was used to evaluate porosity. The ZnO@ZIF-8 isotherm curve is a typical type I adsorption–desorption isotherm that is similar to the porosity of 2.48 nm microporous substances. The ZnO@NA and ZnO@INA isotherm curves seem to be type IV isotherms that also relate to the compounds with porosities of 23.24 and 6.31 nm, respectively. ZnO@ZIF-8, ZnO@NA, and ZnO@INA have BET specific surface areas of 782.695, 77.539, and 13.44 m^2/g, respectively. When compared to simple ZnO nanoparticles, the appearance of zinc oxide NPs in ZnO@MOFs enhances the active surface area (from 1 to 4 m^2/g). ZnO@INA, ZnO@NA, and, ZnO@ZIF-8 have pore sizes ranging from, 4.51 to 6.31 nm, 13.87 to 23.24 nm, and 2.18 to 3.78 nm, respectively [202].

5.5. TEM images of a number of widely used MOFs

The adsorption features of magnetic montmorillonite (MMMT) for Pb(II) are excellent. Shen et al. used *in situ* polymerization to change Zn-BDC, a type of MOF, onto the surface of MMMT to improve its adsorption performance. TEM was used to characterize the nanocomposites MMMT@Zn-BDC. The structures, morphology, and properties of MMMT@Zn-BDC, Zn-BDC, and MMMT were investigated using TEM. Fig. 7a demonstrates Fe_3O_4 nanoparticles that are roughly spherical and MMT anomalous crystalline when the amplified diameter is over 450 nm. The distribution of Fe_3O_4 and MMT is nearly identical. This was affirmed that MMMT had been successfully fabricated. The Zn-BDC crystals in Fig. 7b are also irregular, with a narrow lattice structure. Fig. 7c demonstrates a narrow lattice structure formed after Zn-BDC seems to be created on the MMMT surface. This was ascertained that a narrow lamellar framework had been successfully fabricated [203].

Liu et al. used numerous specific assembly methods to make 3 kinds of ternary MOF-on-MOF nanostructures. Using a solvothermal technique, a tetragonal structured Ti-centered MOF (MIL-125, space group I4/mmm, lattice parameters a = 18.65 and c = 18.14) was produced as the host. The length and width, respectively, are approximated to be 500–640 and 125 nm. The solid character of MIL-125 can be seen in TEM images. The kinds of binary heterostructure seem to have a sandwich-like framework, according to TEM findings. The intermediate Ti-rich layer is sandwiched by two sides Co-rich layers, as seen in the high-angle annular dark-field scanning TEM (HAADF-STEM) and correlating element mapping images seen as perpendicularly to the nanocake top/bottom surface [204].

6. Application of MOFs in the detection of food contaminants and drug ingredients

Electrochemical detection is a powerful analytical technique that involves the conversion of chemical information into electrical signals. In electrochemical detection, the analyte of interest undergoes a redox

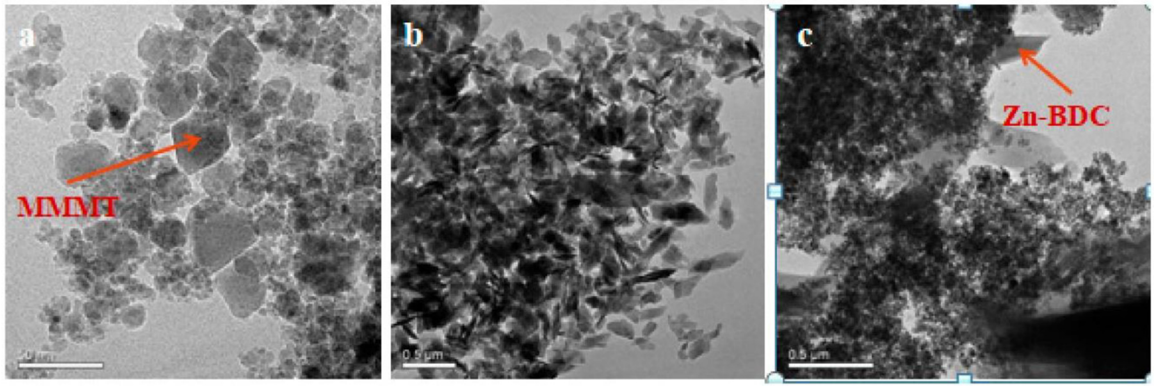

Fig. 7. TEM images of (a) MMMT, (b) Zn-BDC, and (c) MMMT@Zn-BDC. Data reproduced from [203].

reaction at an electrode, which generates a current or voltage signal that is proportional to the concentration of the analyte. The fundamental principles of electrochemical detection are based on the properties of electrodes and the behavior of electrochemical reactions. Electrodes are materials that can conduct electricity and are used to transfer electrons between the analyte and the electrical circuit. Electrodes can be made of various materials, including metals, metal oxides, carbon, and conductive polymers. When an electrode is immersed in a solution containing an analyte, the analyte can undergo a redox reaction with the electrode. Redox reactions involve the transfer of electrons between the analyte and the electrode, resulting in the formation of a reduced or oxidized species. The direction and magnitude of the electron transfer depend on the electrochemical potential difference between the analyte and the electrode. The electrochemical potential difference between the analyte and the electrode can be measured using various electrochemical techniques, including voltammetry, potentiometry, and amperometry. Voltammetry involves the application of a voltage ramp or step to the electrode, while the resulting current is measured. Potentiometry involves the measurement of the potential difference between two electrodes, while amperometry involves the measurement of the current flowing through the electrode. The sensitivity and selectivity of electrochemical detection depend on several factors, including the electrode material, the type of redox reaction, and the measurement technique used. For example, the selectivity of electrochemical detection can be improved by using modified electrodes that can selectively bind to the analyte of interest. Additionally, the sensitivity of electrochemical detection can be enhanced by optimizing the electrode surface area, the applied potential, and the measurement conditions. Electrochemical detection has a wide range of applications in analytical chemistry, including the detection of biomolecules, environmental pollutants, and pharmaceuticals. Electrochemical biosensors, for example, use enzymes or antibodies as recognition elements to selectively detect specific analytes, such as glucose or cholesterol. Electrochemical sensors can also be used for *in situ* monitoring of industrial processes, such as the detection of corrosion or the monitoring of fuel cell performance. Overall, electrochemical detection is a versatile and powerful analytical technique that provides a sensitive and selective means of detecting a wide range of analytes. With continued advances in electrode materials, redox chemistry, and measurement techniques, electrochemical detection is likely to play an increasingly important role in analytical chemistry and other fields in the coming years [205,206].

Electrochemical detection of antibiotics involves using electrochemical sensors to detect the presence and concentration of antibiotics in a sample. Antibiotics are commonly used in medicine and agriculture to treat and prevent bacterial infections, but their overuse can lead to antibiotic resistance, which is a growing global health concern. Therefore, it is important to monitor the levels of antibiotics in various environments, such as food, water, and clinical samples. Electrochemical sensors work by measuring the changes in electrical properties of a material when it interacts with a target analyte. Antibiotics can be detected electrochemically by functionalizing the surface of the sensor with specific receptors or enzymes that can selectively bind to the target antibiotic. When the antibiotic binds to the receptor or enzyme, it causes a change in the electrical properties of the sensor, which can be measured and correlated with the concentration of the antibiotic in the sample. Several electrochemical techniques can be used for antibiotic detection, including cyclic voltammetry, amperometry, and impedance spectroscopy. These techniques offer advantages such as high sensitivity, selectivity, and rapid response times. Additionally, electrochemical sensors can be miniaturized and integrated into portable devices for on-site analysis. Overall, electrochemical detection of antibiotics offers a promising approach for monitoring antibiotic levels in various environments and can contribute to efforts to combat antibiotic resistance [207,208].

Nitrofurazone (5-nitro-2-furaldehyde semi-urea) (NFZ) seems to be a wide antibiotic made from nitrofuran compounds. NFZ is antibacterial and has good resistance to a wide range of Gram-positive and Gram-negative bacteria [209]. It can treat skin problems as well as trypanosomiasis. NFZ can be teratogenic and carcinogenic, and it can be consumed by humans through the food system. The use of NFZ for animals and humans has been prohibited by the Chinese Department of Agriculture. Nevertheless, because of its strong antibacterial quality and reduced cost, NFZ is still widely used illegally. As a result, a quick, sensitive, useful, and effective method of analysis for NFZ data is presented [210]. Electrochemical determination seems to have a cheaper price, easier sample processing, good selectivity, and a quick detection time when compared to all other analysis methods. That many electrochemical sensors, on the other hand, have trouble recognizing a specific sample. As a result, molecular imprinting technology (MIT) must be made to improve the specialized detection performance.

Cheng et al. proposed a new molecularly imprinted electrochemical electrode for nitrofurazone detection that is both sensitive and efficient (NFZ). Cr_2O_3 deduced from an MOF, Ag nanoparticles, and biomass carbon (BC) from walnut shells were used to modify the electrode. Silver nanoparticles are grown on the surface of Cr-MIL-101 to produce Cr-MIL-101/Ag, which is then calcined with BC to produce the nanocomposites BC/Cr_2O_3/Ag. The obtained Cr-MIL-101 seems to have a homogeneous octahedral morphology with a particle diameter of 400 nm, according to SEM and TEM images. On the outside of Cr-MIL-101, Ag Nanoparticles were prepared *in situ*. This substance increases the electrode's efficient surface area and electron transport potential, thereby raising the current response. The application of molecularly imprinted polymer (MIP) toward the surface of nanocomposites could also enhance the specific recognition capacity of modified sensors for NFZ. MIP was synthesized through precipitation polymerization of acrylamide (AM) and methacrylic acid (MAA) as polyfunctional monomer units and NFZ as the framework. The MIP achieved with the precipitation polymerization process creates a spherical shape. Through hydrogen bonding, MIP could ultimately have consequences for NFZ, increasing the sensitivity of modified sensors. Furthermore, the surface of the electrode modified with BC/Cr_2O_3/Ag/MIP is harsh and void-filled. The presence of voids promotes the transfer of electrons and enhances the NFZ's electrochemical performance. The electrochemical performance of bare electrodes and various fabrication sensors was studied using cyclic voltammetry (CV). At 0.2 and 0.3 V, the bare electrode shows two distinct redox signals of potassium ferricyanide. Due to Cr-poor MIL-101′s conductivity, the signal current of the procured CV is determined accordingly. *In situ* growth of Ag NPs on Cr-MIL-101 shows significant improvements in conductivity, demonstrating that the peak intensity of Cr-MIL-101/Ag is greater than that of the unmodified sensor. Cr-MIL-101/Ag had been evidenced upon that BC surface that would improve conductivity and lead to the formation of BC/Cr-MIL-101/Ag. The mixture is then calcined at extreme temps to produce BC/Cr_2O_3/Ag. The BC/Cr_2O_3/Ag curve is significantly greater than the BC/Cr-MIL-101/Ag curve, suggesting that the conductivity is considerably enhanced. It's due to the composite's enhanced effective surface area that enhances the transfer of electrons. The maximum current had been effectively diminished after MIP and NIP were added to add drop-wise to the composite surface. The differential pulse voltammetric (DPV) current response of a modified electrode (BC/Cr_2O_3/Ag/MIP/GCE) to NFZ demonstrated a great linear correlation among 5×10^{-9} to 1×10^{-5} M in the most appropriate experimental situation, and the limit of detection was 3×10^{-9} M. The above technique is extremely reproducible, sensitive, stable, and selective. Furthermore, BC/Cr_2O_3/Ag/MIP/GCE was used to detect NFZ in real samples. To test the appropriateness of BC/Cr_2O_3/Ag/MIP/GCE electrochemical sensors for nitrofurazone in real samples, pharmaceutical agents, urine, drug-free plasma, and used (nitrofura powder). The NFZ recovery of this sensor was determined using standard addition techniques. Before the analysis, the urine and plasma were dissolved 100 times in PBS (pH = 7). The detection method is then preserved under optimal experimental parameters for statistical analysis by gradually adding a solution of NFZ in the dynamic range of the calibration curves. The standard curve was used to measure the composition of spiked NFZ in serum and urine samples. Urine recoveries ranged from 98.20 to 102.84 percent, with a maximum RSD of 4.00 percent. Serum sample recoveries were 98.86 percent, and 103.04 percent and the highest RSD was 4.12 percent. The recovery of NFZ shows that the BC/Cr_2O_3/Ag/MIP/GCE electrochemical electrode can be used to reliably analyze body samples. The BC/Cr_2O_3/Ag/MIP/GCE strategy is a dependable method for determining NFZ in body samples [211].

Diabetes is presently a prevalent infectious disease that poses a significant threat to public health. As a result, establishing a simple and sensitive glucose determination technique is critical for the specific diagnosis and control of diabetes. Nonenzymatic electrochemical glucose diagnosis has attracted widespread attention advantages of Economical, high sensitivity, and simple operation when, especially in comparison to spectroscopy, colorimetry, and fluorescence analytical techniques. Nonenzymatic electrochemical glucose detection is common due to its fast response, simplicity of use, low cost, and repeatability. Zhang et al. initially produced Co-Cu MOFs components using solvothermal methodologies. Secondary solvothermal sulfurization produced several small pores spindle-like Cu-Co sulfide microspheres that maintained the morphological characteristics of the MOFs byproducts. According to electrochemical measurements, the as-synthesized Cu-Co sulfides have awesome nonenzymatic glucose detection capabilities. Because once comparison to CuS, Co(II) ion-doped CuS enhances conductivity and electrochemical performance.

The CV curves of the unmodified electrode and copper-cobalt sulfide-modified sensors in the 0.1 M NaOH electrolytic solution 1 μM Glu-are seen in Fig. 8a. The unmodified electrode seems to not react to glucose, the CuS- and Co-CuS-1-modified sensors have inadequate redox peaks, and the Co-CuS-2-modified electrode seems to have a two of apparently reversible redox at 0.45/0.60 V (vs. Ag/AgCl), suggesting that the Co-CuS-2 sample has the perfect response to glucose. The CV curves of CuS, Co-CuS-1 and Co-CuS-2 at various glucose levels can be seen in Fig. 8b–d, and also the redox peaks of the Co-CuS-2 sensor are the greatest, suggesting that this substance seems to have the perfect electrochemical behavior for glucose of the three specimens. The three major steps can be used to explain the potential redox process of glucose:

$$\mathrm{CuCo-S + OH^- + H_2O \rightarrow CuSOH + CoSOH + e^-}$$

$$\mathrm{CoSOH + OH^- \rightarrow CoSO + H_2O + e^-}$$

$$\mathrm{CuOSH + CoSO + glucose \rightarrow CuS + CoSOH + glucolactone}$$

A LOD of 0.1 M at a potential of 0.55 V, the sensitivity was 1475.97 μA/(mM/cm^2) and the dynamic range of the Co-CuS-2 sensor for glucose detection was 0.001–3.66 μM, which was significantly higher than that of the CuS and Co-CuS-1 specimens. The above research offers an appropriate technique for detecting glucose and created a new avenue for enhancing the electrochemical development of non-enzyme electrochemical sensors [212].

Fentanyl is a particularly successful analgesic and narcotic drug that is extensively used during anesthesia and chronic pain management. Naghian et al. created a straightforward electrochemical approach for detecting fentanyl in the electrolyte solution. A screen-printed carbon electrode (SPCE) was modified by trying to cast a MOF on its surface. To make the modified electrode, Zn(II)-MOF was distributed in Deionized water (5 mg in 2 mL), then 5 μL of the as-prepared suspension was dropped onto the surface of SPCE and dried in an oven at 50 °C. The electrochemical behavior of the as-prepared sensors was evaluated utilizing the cyclic voltammetry (CV) method. Electrochemical properties in a 5 mM $K_3[Fe(CN)_6]/K_4[Fe(CN)_6]$ compound including 0.1 KCl in the potential range of 0.3 to 0.7 V were conducted for this aim. The reduction and oxidation signals of $K_3[Fe(CN)_6]/K_4[Fe(CN)_6]$ at the SPCE surface are really weak. When the sensor was modified with Zn(II)-MOF, a redox signal for the $K_3[Fe(CN)_6]/K_4[Fe(CN)_6]$ solvent revealed a significant improvement of 62 mV, revealing that this sensor has greater ability than the bare sensor. Electrochemical reactions can be influenced by specimen and instrument circumstances including scan rate and solution pH. The influence of scan rates was investigated by measuring the CV of fentanyl (100 M) in PBS solution (0.1 M, pH = 7) at different scan rates ranging from 10 to 200 mV/s. With a slope of 0.735 and a correlation coefficient (*R*2) of 0.981, the linear relationship between the logarithm of the scan rate and the logarithm of the peak current demonstrates both absorption and diffusion behavior of the transfer of electrons on the Zn(II)-MOF/SPCE surface. At the logarithmic scan rate, a Tafel plot was achieved from the measured potential curve. This can be indicated as a two-electrons process by using the slope of potential vs the logarithm of the scan rate (slope = $(1-\alpha)\, nF/2.303\, RT$). Fentanyl had an electron transfer coefficient of 0.67. The catalytic constant (k_s) was also determined using the *E*-log*v* graph and the Laviron equation.

$$\log k_s = \alpha \log(1-\alpha) + (1-\alpha)\log\alpha - \log(RT/nFv) - \alpha(1-\alpha)\left(nF\Delta E_p/2.3\, RT\right)$$

Where the letters *n*, *F*, *R*, and *T* have their usual definitions. The catalytic constant (k_s) was determined using the Laviron equation and found to be 3.081 s^{-1}. The electrochemical performance of fentanyl on the working electrode, on the other hand, was investigated using the DPV approach. The impacts of the scan rate and pH on the cyclic voltammetry (CV) and DPV answers, respectively, were used to determine the best experimental results. Fentanyl seems to have an irreversible performance at a potential of 0.9 V, and its current increases in the appearance of MOF, according to the findings. For fentanyl in an aqueous system, the development of the proposed sensor with the DPV approach revealed a detection limit of 0.3 μM in the range of concentrations of 1–100 μM (dynamic range). The modified electrode was effective in detecting low

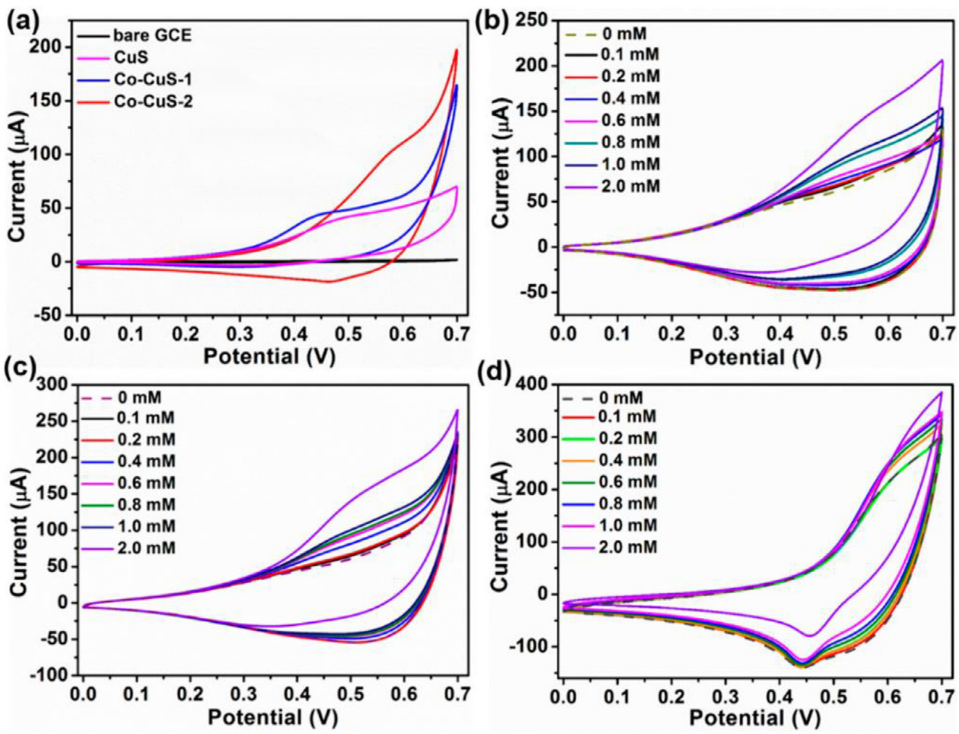

Fig. 8. (a) CV curves of CuS, Co-CuS-1, Co-CuS-2, and unmodified electrode in 0.1 M NaOH electrolyte containing 1 μM Glu (20 mV/s). CV curves in NaOH solution with different glucose concentrations: (b) CuS, (c) Co-CuS-1, and (d) Co-CuS-2 (100 mV/s). Data reproduced from [212].

concentrations of fentanyl in urine and serum, which can be used as real samples [213].

Alsafrani et al. prepared a new category of conductive MOF, polyaniline-aluminum succinate (PANI@Al-SA) nanocomposite, via the oxidation process of aniline monomer with potassium persulfate as an oxidizing agent. The Dc power conductivity of polymer-MOFs was measured using the four-probe technique. The Zn(II) ion was detected using a bare glassy carbon electrode (GCE) modified with Nafion/PANI@Al-SA. Cations are important in many different procedures, including medical, biological, and chemical ones, and they also contribute significantly to environmental damage. The ion Zn(II) has been found in the environment from the manufacture of paper, varnishes and dyes, environmental toxins, and sometimes even medical products, and it is harmful to human health. As a result, an electrochemical sensor must be designed to detect Zn(II) ions concentration regularly. The efficiency of modified electrodes increased by 91.9 percent.

On the voltammetric answer, the supporting electrolyte plays an essential part in the electrochemical reaction. The electrochemical performance of GCE modified with PANI@Al-SA/Nafion to 0.03 mM Zn^{2+} was investigated using 0.1 M acetic acid with a pH of 2.8 and 0.1 M acetate buffer solutions in the pH range of 3.6 to 5. The anodic peak current is enhanced by increasing pH until it reaches its peak value at pH 4.5, as shown in Fig. 9a. In a reduced acidic environment, the electrochemical reaction of zinc ions is beneficially attributed to the impact of hydrogen dissolving in a more acidic condition. As a consequence, subsequent studies used a pH of 4.5 as the ideal pH. Different metal ions with a concentration range of 0.03 μM in 0.1 M acetate buffer moderate at pH 4.5 were assessed to determine the performance behavior of PANI@Al-SA/Nafion modified electrode as a sensing element to zinc ion. The selectivity research of PANI@Al-SA/nafion to Mg^{2+}, Mn^{2+}, Ni^{2+}, Cd^{2+}, Zn^{2+}, and Cu^{2+} is shown in Fig. 9b. When compared to those other metal ions, the anodic peak current to Zn^{2+} was the maximum. This showed that the proposed modified sensor is much more sensitive to zinc ions. Fig. 9c demonstrates that the PANI@Al-SA/Nafion modified GCE has a very well peak current potential of 0.86 V (ipa = 21 A), whereas the unmodified GCE has a reduced peak value (ipa = 6 A). The GCE's electro-catalytic activity was enhanced by the PANI@Al-SA nanocomposite's behavior. Moreover, owing to the presence of PANI@Al-SA on the naked GCE surface, the PANI@Al-SA/Nafion modified GCE sensor demonstrated a perfect cathodic signal in 0.1 M acetate buffer of pH 4.5 (middle except in the apparent lack of Zn^{2+} ion). Throughout this context, the electrochemical reaction of PANI@Al-SA/Nafion modified proposed GCE was compared to that of its constituting PANI and AL-SA in the appearance of analyte zinc ion in the existence of 0.1 M acetate buffer moderate at pH 4.5 as a solvent. As shown in Fig. 9d, PANI@Al-SA/Nafion modified electrode showed an anodic peak value at 23.5 A (Epa = 0.86 V), which is a large current reply when comparison to Al-SA/Nafion modified GCE's anodic current at 18 A (Epa = 0.63 V), whereas PANI/Nafion modified GCE demonstrates no reaction together under the circumstances. The above result revealed that the PANI@Al-SA/Nafion/GCE sensor has unique physical and chemical properties than its components PANI and Al-SA, which is confirmed by the physicochemical performance mentioned in the previous section.

The modified electrode (PANI@Al-SA/Nafion/GCE) had excellent catalytic characteristics such as good Zn(II) ion sensitivity. With a detection limit of LOD 0.59 μM and extremely good sensitivity of 7.14 $\mu M/cm^2$, a linear concentration range of 2.8–228.6 μM was achieved. The constructed operation for detecting Zn(II) ions in a real sample demonstrated excellent repeatability and repeatability and also was unaffected through common interferents. As a result, the advanced process shows potential for measuring Zn(II) ions in bottled and tap water. To assess the dependability of the advanced analysis approach, it was applied to the measurement of zinc ions in real water samples. As shown in Table 1, the findings revealed that positive recoveries were achieved in the area of application, indicating the effectiveness of the suggested sensor for the detection of Zn^{2+} ions in real samples [214].

Yang et al. created a dual-channel electrode platform for ratio metric electrochemical detecting and real-time drug release monitoring. 2-Methylimidazole was produced through the appearance of sulfur nanostructures (SNPs) and cobalt ions to establish SNPs-encapsulated cobalt MOF, SNPs@MOF. By using ultrasound-assisted liquid-phase exfoliation, boron nanosheets (BNSs) were synthesized, then loaded with ferrocene (Fc) to produce the BNSs-Fc structure. A clean GCE was modified with Nafion upon that surface, accompanied by drop-casting of BNSs-

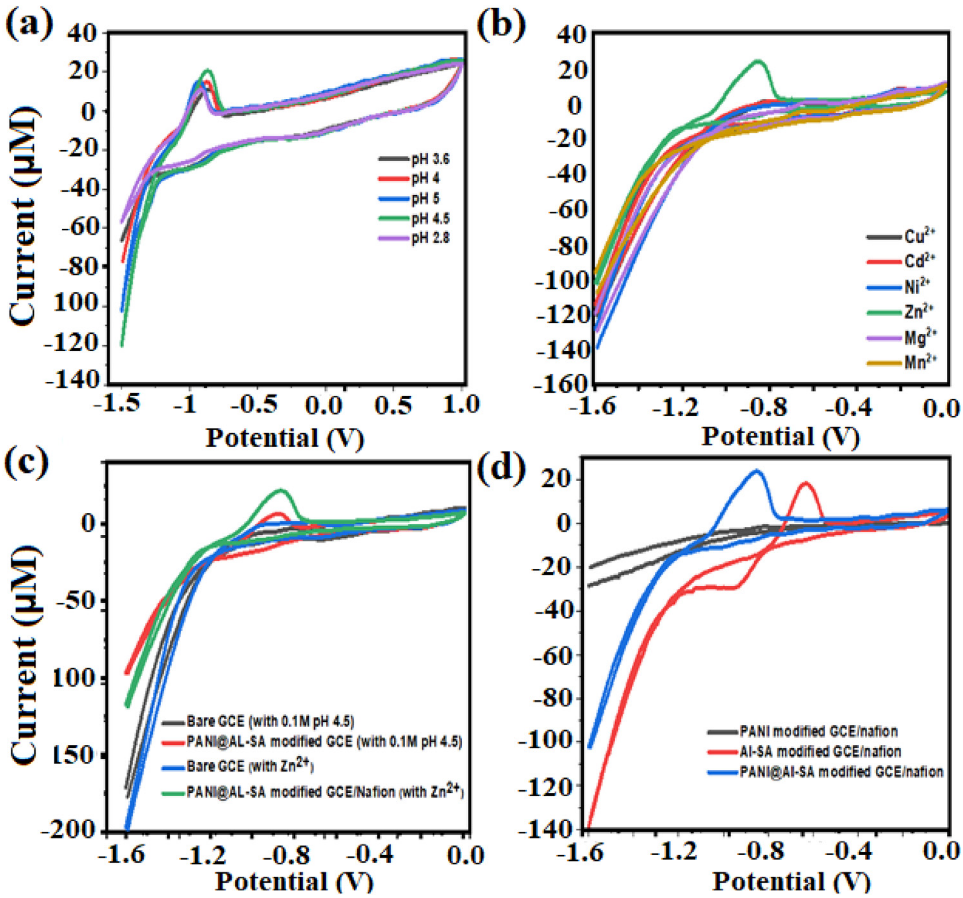

Fig. 9. (a) Cyclic voltammograms of 0.03 μM Zn^{2+} in pH solutions at a scan rate of 100 mV/s. (b) At a scan rate of 100 mV/s, the CV response of PANI@Al-SA/Nafion modified GCE to 0.03 μM of various metal ions in acetate buffer solution at pH 4.5 was compared. (c) At a scan rate of 100 mV/s, CV diagrams of unmodified and PANI@Al-SA/Nafion modified GCE in the appearance and nonappearance of 0.03 μM Zn^{2+} in acetate buffer solution at pH 4.5 were recorded. (d) PANI@Al-SA/Nafion CV response compared to its components in acetate buffer at pH 4.5 contains 0.03 μM Zn^{2+} at 100 mV/s scan rate. Data reproduced from [214].

Table 1
Results collected from the suggested (LSV) approach for determination of zinc ions in real samples Data reproduced from [214].

Sample	Spiked Concentration (μM)	Found Concentration (μM)	RSD (%) (n = 3)	Recovery (%)
Tap water	0	0	–	–
	3	2.94	1.4	98.06
	6	5.8	1	96.11
Bottled water	0	0	–	–
	3	2.91	1.45	97.22
	6	5.86	0.8	97.78

Fc and SNPs@MOF to create a modified electrode platform, SNPs@MOF/BNSs-Fc/GCE. Product crystal structures, morphological characteristics, spectra, and properties were studied in detail. Because of the steady Fc spectrum analyzer and evidenced ADR sensor production during the electrochemical oxidation reaction of Fc and ADR, the framework has been used as an innovative ratiometric-modified electrode for the detection of Adriamycin (ADR). The excellent electroactivity of compounds in the compounds of hydroquinone and Quinone factions makes electrochemical analytical procedures even more appealing.

Also with the addition of ADR, the SNPs@MOF/BNSs-Fc/GCE system was engrossed in Phosphate buffered saline (1 mM, pH 6.5) electrolyte. Square wave voltammetry (SWV) plots were evaluated as the last established [ADR] enhanced. The intensity reduction and oxidation of ADR create IADR to slowly raise, resulting in minor modifications in IFc. Throughout the range of 0.01–10 M, there seems to be a graph (R^2 = 0.9901) linear curve relationship of IADR/IFc vs [ADR]. According to signal-to-noise (S/N = 3) estimations, the LOD is as small as 2 nM. Ratiometric electrochemical sensors are based on the SNPs@MOF/BNSs-Fc/GCE framework was constructed for sensitive detection of ADR in aspects of the linear relationship. Researchers have reported electrochemical sensor technologies of ADR utilizing chemically synthesized sensors, and many of them used output data modes to detect ADR. There has yet to be a study that includes dual-signal ratiometric electrochemical detecting of ADR using chemically modified sensors. The designed ratiometric electrochemical sensor, on the other hand, has an appropriate linear concentration range of [ADR] and a reduced LOD, which seem to be similar and superior to another prior research process. The system-based sensor's unique dual-signal ratiometric production and specific fabrication provide excellent detection performance and achievability throughout detecting objects in biological materials. Under perfect circumstances, the sensor can detect ADR in a wide range of 0.01–10 μM, with a good detection limit of 2 nM. The electrode was found to have high detection selectivity, sensitivity, and stability, and it was able to detect ADR in biological fluid samples, displaying potential practicability and reliability. Furthermore, the proposed BNSs-ADR carriers in liquid electrolytes seem to be capable of random and pH-regulatable ADR release [215].

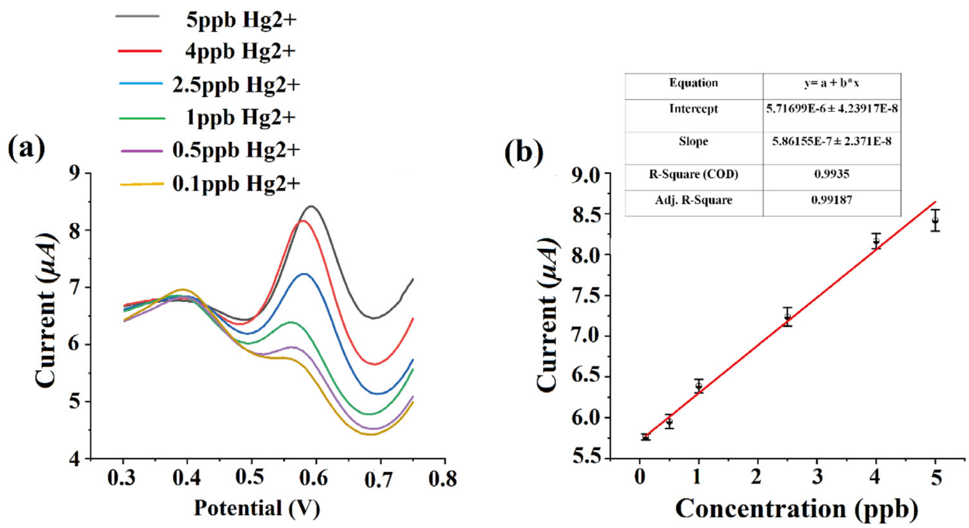

Fig. 10. (a) Current response to various Hg^{2+} concentrations; (b) Hg^{2+} liner response curve. Data reproduced from [216].

Hg^{2+} is a biochemically harmful material that, when ingested, can cause neurological and cognitive disturbances. Although the composition of mercury in water sources is really small, it could pose a hazard to the environment and public health owing to its large enhancement factor (up to 106). Several more nations impose strict legislative action restrictions on its concentration; for example, the United States Environmental Protection Agency (US-EPA) restriction advises that the Hg^{2+} in drinkable water be less than 2 ppb. To detect or supervise trace Hg^{2+} environmental damage in the source water, a precise and on-site technique must be established. Xiong et al. developed an innovative Ru-MOFs modified gold microelectrode configuration for Hg detection. Ru-MOFs were made immediately on a gold working electrode using the cathodic technique, with the area covered carefully governed. Ru-MOFs synthesized by cathodic synthesis have high conductivity and can be used as the electrode specimen surface straight. The sensor's performance was significantly enhanced by combining the pre-deposition and adsorption procedures of Ru-MOFs. They discovered that the Ru-MOFs@Au sensor responds well to detecting Hg, so they used it to diagnose Hg at various concentrations ranging. Fig. 10a depicts the characteristic curve, while Fig. 10b depicts the linear curve. The research revealed that a microelectrode modified with Ru-MOFs could be used to detect trace Hg in an aqueous system. The redox current rises as Hg is enhanced, as can be seen in Fig. 10a, b. With a correlation coefficient of 0.996, the linear dynamic range was 0.1 to 5 ppb. The sensitivity is 0.583 A/ppb/mm^2, and the LOD is 0.08 ppb. Because the entire test system requires only 6 min, this tiny sensor is utilized for detecting mercury quickly. These findings suggested that the proposed electrode could be used to detect vestige Hg in the research area. Most interestingly, the senor seems to have a powerful anti-interference ability and satisfying recoveries. This small electrochemical-modified electrode can detect trace mercury on the spot in the research area. All of the findings revealed that the electrode could be used to detect trace amounts of mercury [216].

As previously mentioned, MOFs have special chemical and physical characteristics that give them the potential for useful applications in the field of electrochemical sensing. Ling et al. created an innovative label-free electrochemical sensing technique for cardiac troponin I (cTnI) based on the immunoaffinity-induced depression of the Cu-MOF-74 electrochemical signal. The electrochemical assay demonstrates that the immunoaffinity reaction among cTnI and anti-cTnI on the surface of the electrode could successfully prevent the electrochemical signal of electrode-confined Cu-MOF-74, implying that the Cu-MOF-74-based interface could be useful in label-free cTnI assessment. Cu-MOF-74 serves as both the immobilization matrix for the probe molecules and the signal source for the sensing analysis in this strategy, making it a bifunctional material. Additionally, the growth of the insulation layer and the obstruction of electrolyte diffusion from the bulk solution to the electrode surface are blamed for the electrochemical signal depression of Cu-MOF-74 caused by the immunoaffinity reaction. The analytical range of cTnI in this method is between 0.01 pg/mL and 1.0 ng/ mL, and the detection limit is 4.5 fg/mL. The Cu-MOF-74-based sensing interface is however trustworthy for cTnI analysis in actual blood serum, demonstrating the biosensor's potential for use in point-of-care testing (POCT) for diseases linked to myocardial injury [217].

Lv et al. developed a sensitive electrochemical sensor for sunset yellow (SY) based on CTAB functionalized graphene (Gr) and Cu/Zr-MOF electrode-modified resources. The CTAB-Gr-Cu/Zr-MOF composites were synthesized by using a mild method and characterized by SEM, FT-IR, and EDX spectrum. The mixture of Cu/Zr-MOF and graphene demonstrated a synergic activity in the oxidation of SY due to the high accumulation efficiency, quick electron transfer percentage, and increased sensing sites. When tried to compare to a bare electrode, the newly developed materials substantially enhanced the electrochemical behavior of SY to 6.53-fold. The oxidation peak currents of SY had a linear relationship with its concentration in a wide range from 0.10 to 8.00 M and 40.00–1000.00 μM under optimized conditions, and the limit of detection was 6.68 nM (S/N = 3). The electrochemical technique has a high sensitivity, stability, and repeatability and has been effectively used to determine SY in soft drinks [218].

Prasanna et al. developed new and more effective manganese cobaltite ($Mn_3Co_3O_4$) and multiwalled carbon nanotube (MWCNT) nanocomposite-based electrochemical sensors for furazolidone (FZD) detection. The co-precipitation method was used to create a binary metal oxide derived from a MOF, and ultrasonication was used to create the $Mn_3Co_3O_4$/MWCNT nanocomposite. Spectrophotometric strategies were used to characterize the prepared $Mn_3Co_3O_4$/MWCNT nanocomposite. Voltammetric assessments were also used to assess the electrochemical performance of the modified electrodes. Remarkably, the LOD and linear range of the $Mn_3Co_3O_4$/MWCNT-modified screen-printed carbon electrode (SPCE) is 0.55 nM and 0.05–650 μM, respectively. The preferential study on FZD was carried out using associated interfering molecules, and the $Mn_3Co_3O_4$/MWCNT/SPCE has suitable storage stability and repeatability. The real-time application of the modified electrode for FZD detection in serum and urine samples was measured with acceptable recovery [219].

7. Investigation of antibacterial applications of MOFs and their composites

Microbial infection is amongst the most complicated issues throughout many fields, including food, pharmaceutics, and the ecosystem, making threats the millions of people's lives globally [81,85,220–222]. According to the WHO, resistance to antibiotics has been one of the best health dangers and a global challenge to the general populace's health as a result of centuries of antibiotic-abusive behavior. As a result, innovative antimicrobial properties must be advanced [91,223]. The evolution of antimicrobial agents has also been classified into three parts: the first-generation antimicrobial agents were organic or inorganic substances and salts, the second-generation antimicrobial agents have always been simple metal compounds and metal ions, and the third-generation antimicrobial agents with configuration. MOFs are classified as antimicrobial agents of the 3rd generation [224]. When compared to conventional bactericidal components, they have a managed ion release efficiency, extendable porosities, higher specific surface area, and a managed ion release efficiency. As a result, MOFs have a promising future in fields such as medical problems, preserving food, treatment of sewage, and antibacterial coating [86,225].

Three-dimensional (3D) Cu-MOFs formed as $[Cu_2(Glu)_2(\text{-L})]$ were prepared by Jo et al. through the hydrothermal method or modified research techniques (Glu-is glutarate, and L is bpy = 4,4′-bipyridine (1), bpa = 1,2-bis(4-pyridyl)ethane (2), bpe = 1,2-bis(4-pyridyl)ethylene (3), and bpp = 1,2-bis(4-pyridyl)propane (4)). Their solid-state constructions could be adjusted mildly to improve their aqueous phase hydrolyzing stability. The antibacterial property of the 4 Cu-MOFs, had been examined by evaluating their minimal bactericidal concentration (MBC) characteristics against 5 bacteria strains, such as MRSA, *S. aureus*, *P. aeruginosa*, *E. coli*, and *K. pneumonia* that are commonly encountered in our everyday lives. Cu-MOFs had been examined for antimicrobial properties against 5 bacteria strains by establishing the MBC amount which resulted in further over 99.9% bacterial killing. Luria Bertani (LB) and agar broth were dissolved in deionized water to make the material. Only regular bacterial proper management was done with new bacteria and LB broth that were cultured at 37 °C on TSA plates. Before actual diagnosis, Cu-MOF 4 had been the foundation in an agate pestle and mortar. Although these Cu-MOFs seem to be systemically extremely stable in an aqueous medium all through antimicrobial activities experiments, they demonstrated great antimicrobial properties against those 5 species of bacteria, such as Gram-negative bacteria (E. coli, K. pneumonia, and P. aeruginosa) and Gram-positive bacteria (*S. aureus* and MRSA) including much reduced MBCs. Instead of the minuscule amount of extractable CuII ionic species, the rigorous 3-dimensional structures with surface active metal sites may play a larger role in neutralizing numerous pathogens and eliminating possible cytotoxicity induced by extractable ionic species [226].

H_2O_2 has long been used to confront infective infectious diseases as among the most popular oxygen radicals. Nevertheless, a high dose of H_2O_2 can cause unwanted toxicity to the healthy body and cell healing to be postponed. Peroxidase-like nanostructures are showing promise enzymes in this respect, thanks to their favorable advancement of H_2O_2's antibacterial achievement whereas attempting to avoid the damage effects due to high H_2O_2 concentrations [227]. Hu et al. used *in situ* reducing to create nanosized Au nanoparticles (UsAuNPs) on extremely thin 2-dimensional MOFs. The resulting UsAuNPs/MOFs combination offers the features of UsAuNPs and ultrathin two-dimensional MOFs, presenting impressive peroxidase-like function in the decomposition of hydrogen peroxide into harmful hydroxyl radicals ($OH^{\cdot}$). With the help of a small concentration of hydroxyl radicals, the as-prepared UsAuNPs/MOFs enzyme demonstrated good antibacterial effects against both Gram-positive (*Staphylococcus aureus*) and Gram-negative *(Escherichia coli*) microbes. Experiments on animals show that this resulting material could efficaciously aid the healing of wounds while also being biocompatible. The above research confirms the antibacterial potential of a combination enzyme and carries significant potential for future biomedical studies [228].

Osteomyelitis is a microbial pathogen that affects the skeletal inflammatory process [229]. Strongly perforated lacerations, disintegrated teeth, or broken bones, are the most common causes. The diagnosis of osteomyelitis is hampered by multi-drug resistance pathogens. As a result of increasing resistance to antibiotics, chronic osteomyelitis can result in amputees or even death. As a result, a separate antibacterial operative with tissue regeneration characteristics could be used as an off-the-shelf product in the diagnosis of osteomyelitis. The pro-osteogenic and antibacterial properties of copper sericin (Cu-SER) MOFs are described in this paper. Comparable to collagen throughout biomineralization in tissue, sericin, a textiles protein with antimicrobial properties and osteoinduction characteristics, behaves as a natural framework for the accumulation of Cu-SER MOFs. As evidenced by mineralization and cell growth (alamarBlue), the MOFs have osteogenic behavior and cytocompatibility in an amount of the drug way (energy dispersive X-ray analysis and Alizarin Red S). Growth kinetic analysis and SEM were used to examine the antibacterial effect of Cu-SER MOFs. Cu-SER MOFs were used to explore how they neutralize the nonlinear properties of microbial cells using the zeta potential. The zeta potentials of undiagnosed *S. aureus* and *E. coli* seem to have been 6.7 and 11.05 mV, respectively. For both bacteria, the zeta quantification of MOF-treated specimens caused considerable differences in interfacial possibility, but not to the identical level. This modification in surface potential (at a concentration of 500 g/mL) is sufficient to disturb the cell membranes, affecting bacterial viability. As a consequence, only this concentration was used to evaluate much more antimicrobial properties. Reduced sericin doses in MOFs (1–3 mg/mL) impeded *E. coli* further than *S. aureus* in growth kinetic analysis in the appearance and nonappearance of Cu-SER MOFs (Fig. 11). The findings shed light on the peculiar property of Cu-SER MOFs, which destroy microorganisms on interaction while being very well considered acceptable by human primary cells. As a result, Cu-SER MOFs can reduce antibiotic reliance [230].

For photodynamic therapy (PDT) of wound infection contaminated with multidrug-resistant (MDR) microbial species, Chen et al. utilized MOFs singly, with no additional antibacterial additives. A simple cation exchange approach is used to combine MOF (PCN-224) NPs with titanium. The photocatalytic efficiency of the procured bimetallic PCN-224(Zr/Ti) for the production of reactive oxygen species under illumination is improved significantly, which is willing to take responsibility for the antimicrobial property. To make a wound dressing with excellent biocompatibility and very little cytotoxicity, PCN-224(Zr/Ti) NPs are filled onto lactic-co-glycolic acid nanostructures. PDT-based *in vivo* recovery of a wound infection contaminated with MDR bacteria is useful with wound treatment. Greatest notably, this research does not require the use of any extra antimicrobial agents, making it simple and inexpensive, and it specifically investigates the possibility of MOFs as a strong nonantibiotic agent in PDT [231].

There has been a lot of interest in the use of MOFs to produce excellent photocatalytic antibacterial properties. Even so, insufficient absorption of visible light and quick electron-hole recombination are two major obstacles to the effective use of MOFs nanostructures. A brand-new class of MOF nanocomposites was created by Guo et al. to produce exceptional visible light photocatalytic antimicrobial properties. The addition of gold nanorod (AuNR) can significantly increase ZIF-8′s ability to absorb visible light due to the strong localized surface plasmonic resonance effect, which increases the production of reactive oxygen species (ROS). Additionally incorporated into the nanocomposite for the synergistic generation of ROS under visible light illumination were gold nanoclusters (AuNCs), an innovative photosensitizer. Due to the abundant generation of ROS, the procured AuNR@ZIF-8@AuNCs nanocomposites demonstrated strong photo-bactericidal behavior against *E. coli* and *Staphylococcus aureus* under visible light irradiation. They also showed that these AuNR@ZIF-8@AuNCs nanocomposites are simple to deposit on the fibers of the masks, which outperformed commercial masks in

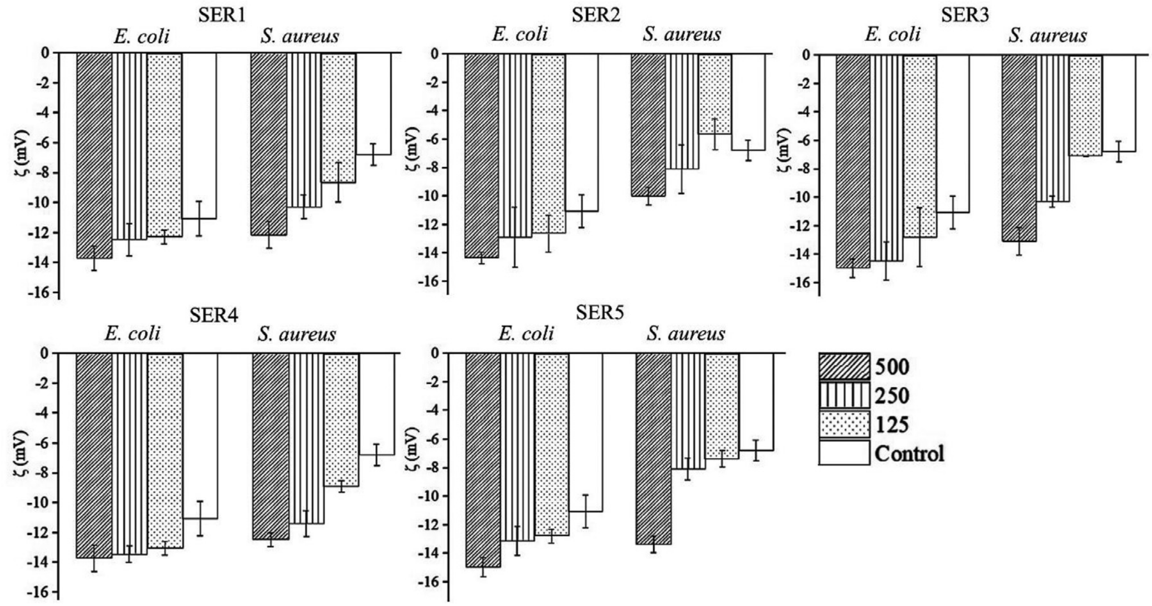

Fig. 11. Effect of treatment of Cu-SER MOFs on bacterial cell surface zeta potential of *Staphylococcus aureus* and *Escherichia coli*. Data reproduced from [230].

terms of antibacterial effectiveness. To improve the photo-bactericidal behavior of MOFs for potential use in the environment and biomedical areas, this study offers a novel plasmon-enhanced method [232].

Traditional metallic antimicrobial nanostructures can cause damage to biological and human organs when metal ions are excessively leached from them [233]. This problem may be resolved by MOFs that coordinate bioactive metal ions to organic bridging linkers, preventing excessive metal ion leaching and simultaneously displaying highly effective antibacterial activities. Li et al. created a 2-dimensional leaves-like zeolitic imidazolate framework (ZIF-L) for antibacterial and anti-algae uses. ZIFs are a type of MOF with a zeolite skeleton structure that consists of an inorganic ligand-transition metal ion and an organic ligand-imidazole or imidazole derivative. The ZIF-L nanosheet completely inactivates *E. coli* (phosphate buffer saline: 4 h) and *Bacillus subtilis* (seawater: 0.5 h). On a wide range of marine algae, the ZIF-L/epoxy material has amazing antibacterial, poisoning, and anti-adhesion properties. It is important to note that by merely adding ZIF-L (0.25 wt%), the percentage removal (*E. coli*) for ZIF/epoxy composite can be increased to 90.20%. Researchers will be motivated by this work to create more MOF materials for use in antibacterial and anti-algae applications [234]. In Fig. 12, the method for creating ZIF-L with a leaf-like morphology was shown.

As the need for food safety grows, it is highly desirable to develop intelligent active packaging films with ammonia-sensitive performance to maintain and monitor the freshness of meat foods [235,236]. Feng et al. successfully synthesized innovative cobalt-based MOFs (Co-MOF) nanostructures with ammonia-sensitive and antibacterial activities, which were then introduced into a sodium alginate (SA) matrix to produce SA-based intelligent active packaging films using the solution casting technique. The impacts of Co-MOF addition on the structure, physical, and functional properties of the SA film were thoroughly investigated. The findings confirmed that the Co-MOF nanofillers were uniformly distributed in the SA composite, resulting in significant improvements in the SA film's tensile strength, toughness, thermal stability, UV shielding, and water vapor barrier capability. Furthermore, the derived SA/Co-MOF composite films demonstrated exceptional antimicrobial properties and ammonia-sensitive discoloration efficiency. The color of SA/Co-MOF composite films changed from pale pink to brownish black when used to monitor shrimp spoilage. These findings suggested that the SA/Co-MOF films developed could be used as intelligent and active materials for packaging food [237].

During indwelling, the anticoagulation and antibacterial capabilities of implant and interventional catheters will establish their failure or success [238]. Zhang et al. used spin coating to create an amino-containing copper-based MOFs (Cu-MOF) coating on the surface of a thermoplastic polyurethane substrate (TPU) for anti-thrombotic and anti-infection impacts. The polyurethane prepolymer coating's (PC) adhesion properties increased the binding force of Cu-MOF particles to the TPU surface and improved stability. It was discovered that a significant amount of NO was loaded in the coating due to the coordination affinity of Cu^{2+} with nitric oxide (NO) and the NO loading capacity of the amino group. All whilst, the coordinated Cu^{2+} in the coating catalyzed endogenous NO donors to generate NO, extending NO release by up to thirty days. Antibacterial tests revealed that the NO released by the coating had antibacterial activities on both *E. coli* and *S. epidermidis*. There is an apparent antibacterial ring visible, and the antibacterial percentage was greater than 96%. It also inhibited platelet adhesion and activation, as well as *in vitro* clotting time and thrombus formation. To summarize, NO release from the covering was achieved for the first time using a combination of NO donor and catalytic endogenous NO donor. It can not only provide the high NO release behavior necessary for the catheter's early anticoagulation and antibacterial properties, but it can also meet standard anticoagulation requirements later on [239].

8. Results and discussion

Various sciences such as mathematics, physics, biology, chemistry, computer, medicine, etc. have faced many advances in recent years [240–266], and nanotechnology is no exception. This article refers to MOFs. A conclusion that can be drawn from the information in this review paper is that MOF-based materials, such as pure MOFs, MOF nanocomposite, and MOF derivative products, have proven to be creative sensing devices for electrochemical sensing uses. When maximizing the effectiveness and utility of the electrochemical experiment, sensitivity and selectivity are crucial factors to take into consideration. Inherent sensitivity for electrochemical detection is provided by the large porosity surface areas of MOFs, which can load the guest molecules and/or catalyze the objectives with significant catalytic performance. Guest molecules can diffuse into the bulk structure thanks to the porosity of MOF-based components, and the size and shape of the pores produce shape- and size-selectivity over the embedded guests. Chemically specific interactions between the guest molecules and MOFs via π-π inter-

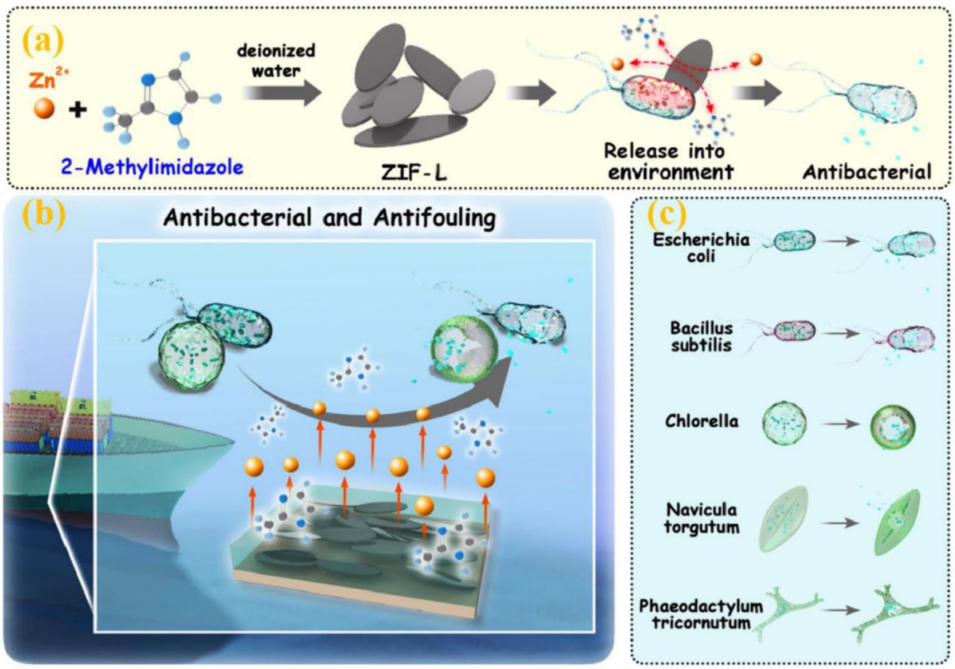

Fig. 12. Schematic illustration of (a) the preparation of ZIF-L and antibacterial mechanism, (b) antifouling and antibacterial effects of ZIF-L-based composites against algae and bacteria, (c) the morphology changes of bacteria and algae after being treated by ZIF-L. Data reproduced from [234].

actions, hydrogen bonding, van der Waals interactions, and open metal sites, are another source of selectivity.

Despite MOFs' interesting properties, which point to them as the perfect components for electrode surface modification, signal transduction is a significant obstacle for MOF-based electrochemical sensors. However, only a percentage of MOFs are used as developed electrode compounds and satisfy the requirements of electrochemical detection. For the properties of MOF-modified electrodes to be used in practical uses, further advancements in redox-active MOF design and conductivity are still needed. Because of their porosity, MOFs can successfully be combined with a variety of functional substances, including carbon nanostructures, metal nanoparticles, biomolecules, and polymers to introduce nonnative conductivity. The electrochemical performances of the MOF composites/hybrids are improved because they combine the benefits of MOFs (high porosity with ordered crystalline pores) and other active materials (electrical and catalytic properties). This would further broaden the applications of electrochemical sensing due to the exceptional qualities of the composite materials resulting from the synergistic combination of both MOFs and compounds [267]. It will be necessary to carefully take into account many of the factors mentioned in this study to optimize the sensing performance when designing MOF-based electrochemical sensors for specific analytes. Despite significant advancements, MOF-based electrochemical sensors are only just beginning to find practical uses. To advance the use of MOF-based nanomaterials of electrochemical sensors, many obstacles still need to be overcome.

We firmly believe that MOF-based components have special advantages and are promising for electrochemical sensing uses, possibly in, but not limited to, the following fields, despite these difficulties and because of the particular structural advantages of MOFs: (1) multiplex detection: creating straightforward multiple analyte detection assays is extremely difficult in terms of practical applications. For example, it is crucial to simultaneously monitor several tumor markers to diagnose cancers correctly and early. It is possible to create distinct electrochemical signals for multiplex detection by using MOFs to create multi-labels or multi-electrode systems. Nevertheless, there is still much to learn about the uses of MOF-based electrochemical sensors for multiplex detection, particularly multiplex antibiotics and/or cancer marker detection [268]. (2) On-site detection is possible by developing MOF-based electrochemical sensors using a screen-printing technique and 3D-printed microfluidic systems. At the moment, an MOF-based electrochemical sensing study is still being developed in a lab [269]. (3) *In vivo* detection: as of now, the majority of research on MOF-based electrochemical biosensors has focused solely on *in vitro* detection. For effective clinical diagnosis and treatments, the *in vivo* detection of biological molecules, biomarkers, etc. is extremely attractive. The first step to achieving the *in vivo* applications may involve creating biocompatible, low-toxicity, and biodegradable MOFs, such as cyclodextrin-based carbohydrate MOFs (CD-MOFs), using endogenous organic linkers or bioactive compounds as surface modifiers [270]. There is still much room for creative research in this fascinating field because the use of MOF-based composites in electrochemical sensors is still in its infancy. For the visualization and characterization of clinical diagnosis and therapy, multifunctional MOF-based components with rational design and controlled fabrication are particularly attractive for combined uses like imaging, biosensing, and controllable drug release. Many innovations are likely to be made in the near future thanks to the collaborative efforts of specialists from various disciplines.

The evolution of antibacterial agents has been separated into three stages: the first-generation antibacterial agents were organic or inorganic mixtures and salts, the second-generation antibacterial agents were simple metal compounds and metal oxides, and the third-generation antibacterial agents with topology [271]. MOFs are antibacterial agents of the third generation. When compared to traditional bactericidal composites, they have a higher specific surface area, an adjustable high porosity, and a controlled ion release percentage. As a result, MOFs have a promising future in food preservation, antibacterial coating, clinical diagnosis, and treatment of wastewater [225]. Due to their mixture, structure, and expensive internal surface volume, MOFs can be used as a reservoir for antibacterial agents, which is one of their benefits as a novel high-performance substance with antibacterial effects. The metal disintegration of the MOFs structures is used to gradually release metal ions to offer a durable antimicrobial property and obtain the costly antibacterial durability of MOFs. In fact, MOFs can be employed as metal ion storage libraries for zinc, silver, nickel, and copper. Additionally, MOFs can incorporate antibacterial compounds into their structure, and their uniform distribution of the metal active sites gives them an advantage over naturally occurring or artificial materials that are weighed down with metal ions. In the course of compound

Table 2
Summary of the characteristics and application of nanoparticles mentioned in the review.

MOF nanocomposites	Synthesis method	Types of ligands	Pore size (nm)	BET surface areas (m^2/g)	Properties and applications	Refs.
$(Cd_3(PDA)_1(tz)_3Cl(H_2O)_4)\cdot 3H_2O$	Slow diffusion	PDA & Tz	–	–	Detection of Pesticides: Experimental and Computational Study	[64]
$([Cu(NPY)_2(DMF)]_2(W_{10}O_{32}))\cdot DMF\cdot 3CH_3CN$	Slow diffusion	NPY	–	–	Photocatalytic oxidation of cyclohexane	[65]
$[[Zn_2(5NO_2\text{-}IP)_2(L)_2](H_2O)]_n$ and $[[Cd_2(5NO_2\text{-}IP)_2(L)_2(H_2O)_4](L)(H_2O)(CH_3OH)_6]_n$	Reflux	IP & L	10–120	10	Reversible dye adsorption	[67]
Mn(II) containing guanidinium-MOF	Reflux	Guanidine carbonate	–	–	Investigation of Structural, thermal and electro-optical properties	[68]
Titanium-based MOFs NH_2_MIL-125 and NTU-9 and MOF NTU-9/NH_2_MIL-125 (HMF)	Reflux	*N,N*-Dimethylformamide (DMF)	–	986, 1267, and 550	Reduction of Cr (VI) from wastewater	[69]
Mn–DABDC	Electrochemical	DABDC	0.353	708 to 590	H_2 and CO_2 uptake	[73]
Mg-MOF-74/MgF_2	Hydrothermal	2,5-dihydroxyterephthalic acid	–	–	Hydrophilicity and Corrosion Resistance	[77]
Cd/Zr-MOF-3 Cd/Zr-MOF-5 Cd/Zr-MOF-7	Hydrothermal	H_2BDC	3.47 4.13 6.95	103.40 91.40 32.78	Enhanced photochemical properties	[78]
MOF-525 and MOF-545	Sonochemical	Tetrakis (4-carboxyphenyl)-porphyrin (TCPP)	2.1 & 3.9	2511	catalytic and adsorption properties	[82]
TMU-16-NH_2/GO	Sonochemical		0.3	258	Investigation of various forthcoming industrial and technological applications	[83]
Fe@MOF-5	Coprecipitation	tetraethyl orthosilicate (TEOS)	–	–	Determination by HPLC	[84]
Fe_2Ni-MIL-88B	Thermal decomposition	Terephthalic acid (H_2BDC)	2–20	390		[86]

Table 3
A summary of papers related to modified electrodes with MOFs for the determination of various compounds.

Sample	Electrode	Detected compounds	LDR (μM)	LOD (μM)	Refs.
1	BC/Cr_2O_3/MIP	Nitrofurazone	10–50	0.003	[211]
2	Co-CuMOF	Glucose	0.001–3.66	0.1	[212]
3	Zn(II)-MOF	Fentanyl	1–100	0.3	[213]
4	Nafion/PANI@Al-SA	Zn(II) ion	2.8–228.6	0.59	[214]
5	SNPs@CoMOF/BNSS-Fc	Adriamycin (ADR)	0.01–10	0.002	[215]
6	Ru-MOF@Au	Hg^{2+}	0.00005–0.025	0.004	[216]
7	Cu-MOF-74	Cardiac troponin I (CTnI)	0.01pg/mL–1 ng/mL	4.5fg/mL	[106]
8	Cu/ZrMOF	Sunset yellow (SY)	40–1000	0.00668	[107]
9	$Mn_3Co_3O_4$drived MOF/MWCNT	Furazolidone (FZD)	0.05–650	0.00055	[108]

deterioration, the MOF metal release mechanism does not change. Moreover, the organic linkers that are used to create MOFs themselves might also be antibacterial. In order to create a synergistic interaction between the metal ions and the organic ligand's antimicrobial properties, linker molecules can be saved in the structure of MOFs. The use of MOFs in the food industry, however, is still in the exploratory phase. There has been little study done on the antibacterial uses of MOFs, such as using them to disinfect water for drinking, along with waste material and possible food protection. It has been suggested that MOFs could be used as a food protectant or food packaging by combining them with healthy antimicrobial compounds, which offers a promising direction for expanding the application of MOFs in the food industry. Recently, it has been reported that food-grade substances can be used to create MOFs and use in the antibacterial investigation. The development of MOFs and their composite materials with broad-spectrum antibacterial, maximum loading percentage, excellent biocompatibility, and other benefits in the food research area for antibacterial application will be a promising trend as antibacterial research on MOFs develops (Tables 2 and 3).

9. Conclusion

MOFs are amazing systems with well-known architecture that can be constructed with high reproducibility and conductivity. The use of MOFs to make sensors is still in its infant stages, and there are a plethora of application fields for such components to explore. MOF components have been evidenced as advanced sensor systems for electroanalytical application fields, such as MOF nanocomposite, pristine MOFs, and MOF derivative products. MOFs have many benefits in the manufacturing of sensing devices due to their inherent properties. This review looks at the structure, synthesis methods, characterization, and current developments in MOF-based components in this growing field, with a focus on the structure, property, application connection, and various ways to enhance the selectivity, sensitivity, reliability, and stability of MOF-based electrochemical devices. MOFs have gotten a lot of press recently because of their potent antibacterial properties. MOFs are also excellent candidates for biomedical uses because of their high biocompatibility and biodegradability. Moreover, due to the ease with which MOFs can be functionalized, multiple nanomaterials with exceptional characteristics can be created, publicizing antibacterial application forms through a synergetic effect. Photo-thermal impact, metal agents and linkers for sterilization, Physical interaction, oxidative, and synergistic effect are among the significant antibacterial processes of MOFs and MOF-derived nanostructures. A wide range of MOFs and MOF-based components were investigated as antimicrobial agents in biology and medicine and varied incarnations, including independent MOFs, combination MOFs, MOFs membrane, MOFs as antibacterial agent delivery vehicles, enzymes. Even though significant progress on MOFs-based components for antibacterial uses has been made, a few issues and challenges should be proposed for future research.

Declaration of Competing Interest

The authors declare that they have no known competing financial interests or personal relationships that could have appeared to influence the work reported in this paper.

References

[1] Dang W, et al. AuNPs-NH_2/Cu-MOF modified glassy carbon electrode as enzyme-free electrochemical sensor detecting H_2O_2. J Electroanal Chem 2020;856:113592.
[2] Safaei M, et al. A review on metal-organic frameworks: synthesis and applications. TrAC Trends Anal Chem 2019;118:401–25.
[3] Zhao D, et al. On reverse degree based topological indices of polycyclic metal organic network. Polycycl Aromat Compd 2022;42(7):4386–403.
[4] Ameen F, et al. Antioxidant, antibacterial and anticancer efficacy of Alternaria chlamydospora-mediated gold nanoparticles. Appl Nanosci 2023;13(3):2233–40.
[5] Liu B, et al. Metal-organic frameworks functionalized with nucleic acids and amino acids for structure-and function-specific applications: a tutorial review. Chem Eng J 2022;428:131118.
[6] Rossin A. Editorial for special issue "Functional coordination polymers and metal–organic frameworks. Multidisciplinary Digital Publishing Institute; 2021. p. 33.
[7] Kitagawa S. Metal–organic frameworks (MOFs). Chem Soc Rev 2014;43(16):5415–18.
[8] Ahmad I, et al. Solution of multi-term time-fractional PDE models arising in mathematical biology and physics by local meshless method. Symmetry 2020;12(7):1195.
[9] Chu YM, et al. On zagreb type molecular descriptors of ceria oxide and their applications. J Cluster Sci 2021:1–10.
[10] Siddiqui MK, et al. On topological descriptors of ceria oxide and their applications. Main Group Met Chem 2021;44(1):103–16.
[11] Pan C, et al. Inhibitory effect of cinnamaldehyde on Fusarium solani and its application in postharvest preservation of sweet potato. Food Chem 2023;408:135213.
[12] Khan MB, et al. Some new classes of preinvex fuzzy-interval-valued functions and inequalities. Int J Comput Intell Syst 2021;14(1):1403–18.
[13] Khan MB, et al. Higher-order strongly preinvex fuzzy mappings and fuzzy mixed variational-like inequalities. Int J Comput Intell Syst 2021;14(1):1856–70.
[14] Ramesh K, et al. Bioconvection assessment in Maxwell nanofluid configured by a Riga surface with nonlinear thermal radiation and activation energy. Surf Interfaces 2020;21:100749.
[15] Khan MI, et al. Significance of temperature-dependent viscosity and thermal conductivity of Walter's B nanoliquid when sinusodal wall and motile microorganisms density are significant. Surf Interfaces 2021;22:100849.
[16] Nazeer M, et al. Multi-phase flow of Jeffrey fluid bounded within magnetized horizontal surface. Surf Interfaces 2021;22:100846.
[17] Ejaz ST, et al. The numerical solution of fourth order nonlinear singularly perturbed boundary value problems via 10-point subdivision scheme based numerical algorithm. AIP Adv 2020;10(9):095322.
[18] Abbas A, et al. Computational study of the coupled mechanism of thermophoretic transportation and mixed convection flow around the surface of a sphere. Molecules 2020;25(11):2694.
[19] Ahmed N, et al. Radiative colloidal investigation for thermal transport by incorporating the impacts of nanomaterial and molecular diameters (dNanoparticles, dFluid): applications in multiple engineering systems. Molecules 2020;25(8):1896.
[20] Ibrahim M, et al. Numerical investigation and ANN modeling of the effect of single-phase and two-phase analysis of convective heat transfer of nanofluid in a cavity. J Therm Anal Calorim 2021;145(4):1969–91.
[21] Madhukesh J, et al. Numerical simulation of AA7072-AA7075/water-based hybrid nanofluid flow over a curved stretching sheet with Newtonian heating: a non–Fourier heat flux model approach. J Mol Liq 2021;335:116103.
[22] Zhang L, et al. Effect of bimetallic modification on blast furnace slag and its application in low-temperature selective catalytic reduction. J Chem Technol Biotechnol 2023;98(4):949–57.
[23] Zhao Y, et al. Nitrogen recovery through fermentative dissimilatory nitrate reduction to ammonium (DNRA): carbon source comparison and metabolic pathway. Chem Eng J 2022;441:135938.
[24] Wang Y, et al. Non-free Fe dominated PMS activation for enhancing electro-Fenton efficiency in neutral wastewater. J Electroanal Chem 2023;928:117062.
[25] Ibrahim M, et al. Investigation of dynamical behavior of 3LPT protein-water molecules interactions in atomic structures using molecular dynamics simulation. J Mol Liq 2021;329:115615.
[26] Dustigeer G, et al. On multiplicative degree based topological indices for planar octahedron networks. Main Group Met Chem 2020;43(1):219–28.
[27] Sargazi S, et al. Application of titanium dioxide nanoparticles in photothermal and photodynamic therapy of cancer: an updated and comprehensive review. J Drug Deliv Sci Technol 2022:103605.
[28] Sargazi, S. and S. Er, Sacide Gelen, S., Rahdar, A., Bilal, M., Arshad, R., et al., 2022.
[29] Sargazi S, et al. Aptamer-conjugated carbon-based nanomaterials for cancer and bacteria theranostics: a review. Chem Biol Interact 2022;361:109964.
[30] Adnan, et al. Impacts of freezing temperature based thermal conductivity on the heat transfer gradient in nanofluids: applications for a curved Riga surface. Molecules 2020;25(9):2152.
[31] Ikram MD, et al. MHD flow of a Newtonian fluid in symmetric channel with ABC fractional model containing hybrid nanoparticles. Comb Chem High Throughput Screen 2022;25(7):1087–102.
[32] Rasool G, et al. Optimal homotopic exploration of features of cattaneo-christov model in second grade nanofluid flow via Darcy-Forchheimer medium subject to viscous dissipation and thermal radiation. Comb Chem High Throughput Screen 2022;25(14):2485–97.
[33] Ali V, et al. Navigating the effect of tungsten oxide nano-powder on ethylene glycol surface tension by artificial neural network and response surface methodology. Powder Technol 2021;386:483–90.
[34] Li F, et al. Melting process of nanoparticle enhanced PCM through storage cylinder incorporating fins. Powder Technol 2021;381:551–60.
[35] Khan MI, et al. Modeling and numerical analysis of nanoliquid (titanium oxide, graphene oxide) flow viscous fluid with second order velocity slip and entropy generation. Chin J Chem Eng 2021;31:17–25.
[36] Chu YM, et al. Degree-based topological aspects of polyphenylene nanostructures. Polycycl Aromat Compd 2022;42(5):2591–606.
[37] Chu YM, et al. Influence of hybrid nanofluids and heat generation on coupled heat and mass transfer flow of a viscous fluid with novel fractional derivative. J Therm Anal Calorim 2021;144:2057–77.
[38] Zhang L, et al. Effect of bimetallic modification on blast furnace slag and its application in low-temperature selective catalytic reduction. J Chem Technol Biotechnol 1986:2023.
[39] Chu YM, et al. Photocatalytic pretreatment of commercial lignin using TiO2-zno nanocomposite-derived advanced oxidation processes for methane production synergy in lab scale continuous reactors. Catalysts 2021;11(1):54.
[40] Megarajan S, et al. Synthesis of N-myristoyltaurine stabilized gold and silver nanoparticles: assessment of their catalytic activity, antimicrobial effectiveness and toxicity in zebrafish. Environ Res 2022;212:113159.
[41] Du J, et al. Application of two-dimensional layered Mo-MOF@ ppy with high valency molybdenum in lithium-ion batteries. Colloids Surf A 2022;632:127810.
[42] Indhira D, et al. Biomimetic facile synthesis of zinc oxide and copper oxide nanoparticles from Elaeagnus indica for enhanced photocatalytic activity. Environ Res 2022;212:113323.
[43] Ameen F, Dawoud T, AlNadhari S. Ecofriendly and low-cost synthesis of ZnO nanoparticles from Acremonium potronii for the photocatalytic degradation of azo dyes. Environ Res 2021;202:111700.
[44] Khan U, et al. γ-Nanofluid thermal transport between parallel plates suspended by micro-cantilever sensor by incorporating the effective Prandtl model: applications to biological and medical sciences. Molecules 2020;25(8):1777.
[45] Moghadam NCZ, et al. Nickel oxide nanoparticles synthesis using plant extract and evaluation of their antibacterial effects on Streptococcus mutans. Bioprocess Biosyst Eng 2022;45(7):1201–10.
[46] Alshehrei F, Al-Enazi NM, Ameen F. Vermicomposting amended with microalgal biomass and biochar produce phytopathogen-resistant seedbeds for vegetables. Biomass Convers Biorefin 2021:1–8.
[47] Sonbol H, et al. Padina boryana mediated green synthesis of crystalline palladium nanoparticles as potential nanodrug against multidrug resistant bacteria and cancer cells. Sci Rep 2021;11(1):1–19.
[48] Mohammad WT, et al. Plant-mediated synthesis of sphalerite (ZnS) quantum dots, Th1-Th2 genes expression and their biomedical applications. S Afr J Bot 2023;155:127–39.
[49] Zhang Y, et al. Optimization of a MOF blended with modified polyimide membrane for high-performance gas separation. Membranes 2022;12(1):34.
[50] Barani M, et al. In silico and *in vitro* study of magnetic niosomes for gene delivery: the effect of ergosterol and cholesterol. Mater Sci Eng C 2019;94:234–46.
[51] Sargazi S, et al. F127/cisplatin microemulsions: *in vitro, in vivo* and computational studies. Appl Sci 2021;11(7):3006.
[52] Rahim M, et al. Nutratherapeutics approach against cancer: tomato-mediated synthesised gold nanoparticles. IET Nanobiotechnol 2018;12(1):1–5.
[53] Alijani HQ, et al. Biosynthesis of core–shell α-Fe_2O_3@ Au nanotruffles and their biomedical applications. Biomass Convers Biorefin 2022:1–15.

[54] Huang S, et al. Template-controlled *in-situ* growing of NiCo-MOF nanosheets on Ni foam with mixed linkers for high performance asymmetric supercapacitors. Appl Surf Sci 2022;572:151344.
[55] Rashti A, et al. Tuning MOF-derived Co_3O_4/$NiCo_2O_4$ nanostructures for high-performance energy storage. ACS Appl Energy Mater 2021;4(2):1537–47.
[56] Arkaban H, et al. Polyacrylic acid nanoplatforms: antimicrobial, tissue engineering, and cancer theranostic applications. Polymers 2022;14(6):1259.
[57] Liu W, et al. Treatment of CrVI-containing $Mg(OH)_2$ nanowaste. Angew Chem Int Ed 2008;120(30):5701–4.
[58] Selvam K, et al. Laccase production from Bacillus aestuarii KSK using Borassus flabellifer empty fruit bunch waste as a substrate and assessing their malachite green dye degradation. J Appl Microbiol 2022;133(6):3288–95.
[59] Ma Y, et al. A sensitive enzyme-free electrochemical sensor based on a rod-shaped bimetallic MOF anchored on graphene oxide nanosheets for determination of glucose in huangshui. Anal Methods 2023;15:2417–26.
[60] Sargazi S, et al. Can nanomaterials support the diagnosis and treatment of human infertility? A preliminary review. Life Sci 2022;299:120539.
[61] Rahdar A, et al. Pluronic F127/carfilzomib-based nanomicelles as promising nanocarriers: synthesis, characterization, biological, and in silico evaluations. J Mol Liq 2022;346:118271.
[62] Lu B, et al. State of the art in CRISPR/Cas system-based signal conversion and amplification applied in the field of food analysis. Trends Food Sci Technol 2023;135:174–89.
[63] Barani M, et al. Aptamer-conjugated carbon nanotubes or graphene for targeted cancer therapy and diagnosis. In: Aptamers engineered nanocarriers for cancer therapy. Elsevier; 2023. p. 277–94.
[64] Mirzaiebadizi A, et al. An intelligent DNA nanorobot for detection of MiRNAs cancer biomarkers using molecular programming to fabricate a logic-responsive hybrid nanostructure. Bioprocess Biosyst Eng 2022;45(11):1781–97.
[65] Rao MP, et al. Synthesis of N-doped potassium tantalate perovskite material for environmental applications. J Solid State Chem 2018;258:647–55.
[66] Kumar V, et al. Evaluation of cytotoxicity and genotoxicity effects of refractory pollutants of untreated and biomethanated distillery effluent using Allium cepa. Environ Pollut 2022;300:118975.
[67] Yang Y, et al. Nanoporous gold embedded ZIF composite for enhanced electrochemical nitrogen fixation. Angew Chem Int Ed 2019;58(43):15362–6.
[68] Zhou M, et al. Hematite nanoparticle decorated MIL-100 for the highly selective and sensitive electrochemical detection of trace-level paraquat in milk and honey. Sens Actuators B 2023;376:132931.
[69] Wang J, et al. An electrochemical sensor based on MOF-derived NiO@ ZnO hollow microspheres for isoniazid determination. Microchim Acta 2020;187(7):1–8.
[70] Wang X, et al. Electrochemical sensor for determination of bisphenol A based on MOF-reduced graphene oxide composites coupled with cetyltrimethylammonium bromide signal amplification. Ionics 2020;26(6):3135–46.
[71] Zhang Z, et al. Electrochemical electrophilic bromination/spirocyclization of N-benzyl-acrylamides to brominated 2-azaspiro [4.5] decanes. Green Chem 2023;25:3543–8.
[72] Wan Q, et al. Recent advances in electrochemical generation of 1, 3-dicarbonyl radicals from C–H bonds. Org Chem Front 2023;1(1):1–16.
[73] Daniel M, et al. MOF based electrochemical sensors for the detection of physiologically relevant biomolecules: an overview. Coord Chem Rev 2022;468: 214627.
[74] Roostaee M, Sheikhshoaie I. Magnetic nanoparticles; synthesis, properties and electrochemical application: a review. Curr Biochem Eng 2020;6(2):91–102.
[75] Roostaee M, Sheikhshoaei I, Karimi-Maleh H. Fe_3O_4@ Au-rGO nanocomposite/ionic liquid modified sensor for ultrasensitive and selective sensing of doxorubicin. Top Catal 2022;65:633–42.
[76] Yusoff N. Graphene–polymer modified electrochemical sensors. In: Graphene-Based electrochemical sensors for biomolecules. Elsevier; 2019. p. 155–86.
[77] Karimi-Maleh H, et al. Carbon paste modified electrode as powerful sensor approach determination of food contaminants, drug ingredients, and environmental pollutants: a review. Curr Anal Chem 2019;15(4):410–22.
[78] Tajik S, et al. Recent developments in electrochemical sensors for detecting hydrazine with different modified electrodes. RSC Adv 2020;10(51):30481–98.
[79] Buledi JA, et al. Current perspective and developments in electrochemical sensors modified with nanomaterials for environmental and pharmaceutical analysis. Curr Anal Chem 2022;18(1):102–15.
[80] Li Y, et al. How effective are metal nanotherapeutic platforms against bacterial infections? A comprehensive review of literature. Int J Nanomed 2023:1109–28.
[81] Subramaniyan SB, et al. Phytolectin-cationic lipid complex revive ciprofloxacin efficacy against multi-drug resistant uropathogenic Escherichia coli. Colloids Surf A 2022;647:128970.
[82] Wang Y, et al. Antibiotic-free antibacterial strategies enabled by nanomaterials: progress and perspectives. Adv Mater 2020;32(18):1904106.
[83] Yang K, et al. Dysfunction of FadA-cAMP signalling decreases Aspergillus flavus resistance to antimicrobial natural preservative Perillaldehyde and AFB1 biosynthesis. Environ Microbiol 2022;24(3):1590–607.
[84] Li YX, et al. Antimicrobial mechanisms of spice essential oils and application in food industry. Food Chem 2022:132312.
[85] Yang R, et al. Membrane-targeting neolignan-antimicrobial peptide mimic conjugates to combat methicillin-resistant Staphylococcus aureus (MRSA) infections. J Med Chem 2022;65(24):16879–92.
[86] Sonbol H, et al. Bioinspired synthesize of CuO nanoparticles using Cylindrospermum stagnale for antibacterial, anticancer and larvicidal applications. Appl Nanosci 2021;13:917–27.
[87] Ameen F, et al. Anti-oxidant, anti-fungal and cytotoxic effects of silver nanoparticles synthesized using marine fungus Cladosporium halotolerans. Appl Nanosci 2021;13:623–31.
[88] Li T, et al. Ecological insight into antibiotic resistome of ion-adsorption rare earth mining soils from south China by metagenomic analysis. Sci Total Environ 2023;872:162265.
[89] Qiu H, et al. Depriving bacterial adhesion-related molecule to inhibit biofilm formation using CeO2-decorated metal-organic frameworks. Small 2019;15(36):1902522.
[90] Amin KM, et al. Antimicrobial ZnO nanoparticle–doped polyvinyl alcohol/pluronic blends as active food packaging films. Part Part Syst Charact 2020;37(4):2000006.
[91] Begum I, et al. A combinatorial approach towards antibacterial and antioxidant activity using tartaric acid capped silver nanoparticles. Processes 2022;10(4):716.
[92] Ibrahim M, et al. Two-phase analysis of heat transfer and entropy generation of water-based magnetite nanofluid flow in a circular microtube with twisted porous blocks under a uniform magnetic field. Powder Technol 2021;384:522–41.
[93] Ibrahim M, et al. Comprehensive study concerned graphene nano-sheets dispersed in ethylene glycol: experimental study and theoretical prediction of thermal conductivity. Powder Technol 2021;386:51–9.
[94] Li J, et al. Heat recovery application of nanomaterial with existence of turbulator. J Mol Liq 2021;326:115268.
[95] Xiong PY, et al. Nanomaterial transportation and exergy loss modeling incorporating CVFEM. J Mol Liq 2021;330:115591.
[96] Xiong PY, et al. Nanoparticles for phase change process of water utilizing FEM. J Mol Liq 2021;334:116096.
[97] Chu YM, et al. Nanoparticle enhanced PCM exergy loss and thermal behavior by means of FVM. J Mol Liq 2020;320:114457.
[98] Shen XY, et al. Molecular dynamics simulation of water-based Ferro-nanofluid flow in the microchannel and nanochannel: effects of number of layers and material of walls. J Mol Liq 2021;338:116924.
[99] Zhou SS, et al. Augmentation of performance of system with dispersion of nanoparticles inside PCM. J Mol Liq 2021;333:115921.
[100] Saqib M, et al. Symmetric MHD channel flow of nonlocal fractional model of BTF containing hybrid nanoparticles. Symmetry 2020;12(4):663.
[101] Ge-JiLe H, et al. Double diffusive convection and Hall effect in creeping flow of viscous nanofluid through a convergent microchannel: a biotechnological applications. Comput Methods Biomech Biomed Eng 2021;24(12):1326–43.
[102] Lund LA, et al. Temporal stability analysis of magnetized hybrid nanofluid propagating through an unsteady shrinking sheet: partial slip conditions. Comput Mater Contin 2020;66(2):1963–75.
[103] Ashraf M, et al. Computational analysis of the effect of nano particle material motion on mixed convection flow in the presence of heat generation and absorption. CMC-Comput Mater Contin 2020;65(2):1809–23.
[104] Haq F, et al. Modeling and theoretical analysis of gyrotactic microorganisms in radiated nanomaterial Williamson fluid with activation energy. J Mater Res Technol 2020;9(5):10468–77.
[105] Khan MI, et al. Exploration of Lorentz force on a paraboloid stretched surface in flow of Ree-Eyring nanomaterial. J Mater Res Technol 2020;9(5):10265–75.
[106] Yang M, et al. Research on microscale skull grinding temperature field under different cooling conditions. Appl Therm Eng 2017;126:525–37.
[107] Almansob A, et al. Effective treatment of resistant opportunistic fungi associated with immuno-compromised individuals using silver biosynthesized nanoparticles. Appl Nanosci 2022;12(12):3871–82.
[108] Sana G, et al. Harmonically convex fuzzy-interval-valued functions and fuzzy-interval Riemann-Liouville fractional integral inequalities. Int J Comput Intell Syst 2021;14:1809–22.
[109] Ibrahim M, et al. The atomic interactions between Histone and 3LPT protein using an equilibrium molecular dynamics simulation. J Mol Liq 2021;328:115397.
[110] Chu YM, et al. Cattaneo-Christov double diffusions (CCDD) in entropy optimized magnetized second grade nanofluid with variable thermal conductivity and mass diffusivity. J Mater Res Technol 2020;9(6):13977–87.
[111] Sahoo S, et al. New soliton solutions of fractional Jaulent-Miodek system with symmetry analysis. Symmetry 2020;12(6):1001.
[112] Riaz M, et al. q-Rung orthopair fuzzy geometric aggregation operators based on generalized and group-generalized parameters with application to water loss management. Symmetry 2020;12(8):1236.
[113] Körpinar T, et al. New uniform motion and Fermi–Walker derivative of normal magnetic biharmonic particles in Heisenberg space. Symmetry 2020;12(6):1017.
[114] Riaz M, et al. Linear Diophantine fuzzy soft rough sets for the selection of sustainable material handling equipment. Symmetry 2020;12(8):1215.
[115] Kalsoom H, et al. Post quantum integral inequalities of Hermite-Hadamard-type associated with Co-ordinated higher-order generalized strongly pre-Invex and quasi-pre-invex mappings. Symmetry 2020;12(3):443.
[116] Chu YM, et al. Thermophoretic particles deposition features in thermally developed flow of Maxwell fluid between two infinite stretched disks. J Mater Res Technol 2020;9(6):12889–98.
[117] Zhong JF, et al. Investigation of Ferro-nanofluid flow within a porous ribbed microchannel heat sink using single-phase and two-phase approaches in the presence of constant magnetic field. Powder Technol 2021;387:251–60.
[118] Ibrahim M, et al. Numerical evaluation of exergy efficiency of innovative turbulators in solar collector filled with hybrid nanofluid. J Therm Anal Calorim 2021;145:1559–74.
[119] Ibrahim M, et al. The effects of L-shaped heat source in a quarter-tube enclosure filled with MHD nanofluid on heat transfer and irreversibilities, using LBM: numerical data, optimization using neural network algorithm (ANN). J Therm Anal Calorim 2021;144:2435–48.

[120] Yang M, et al. Predictive model of convective heat transfer coefficient in bone micro-grinding using nanofluid aerosol cooling. Int Commun Heat Mass Transf 2021;125:105317.
[121] Ibrahim M, et al. Energetic and exergetic analysis of a new circular micro-heat sink containing nanofluid: applicable for cooling electronic equipment. J Therm Anal Calorim 2021;145:1547–57.
[122] Ibrahim M, et al. Using artificial neural networks to predict the rheological behavior of non-Newtonian graphene–ethylene glycol nanofluid. J Therm Anal Calorim 2021;145:1925–34.
[123] Khan U, et al. Impact of Smoluchowski temperature and Maxwell velocity slip conditions on axisymmetric rotated flow of hybrid nanofluid past a porous moving rotating disk. Nanomaterials 2022;12(2):276.
[124] Ge-JiLe H, et al. Three-dimensional radiative bioconvective flow of a sisko nanofluid with motile microorganisms. Coatings 2021;11(3):335.
[125] Chung JD, et al. Partially ionized hybrid nanofluid flow with thermal stratification. J Mater Res Technol 2021;11:1457–68.
[126] Shah Z, et al. Design of neural network based intelligent computing for neumerical treatment of unsteady 3D flow of Eyring-Powell magneto-nanofluidic model. J Mater Res Technol 2020;9(6):14372–87.
[127] Abbas SZ, et al. Modeling and analysis of unsteady second-grade nanofluid flow subject to mixed convection and thermal radiation. Soft Comput 2022;26:1033–42.
[128] Chu YM, et al. Topological properties of polycyclic aromatic nanostars dendrimers. Polycycl Aromat Compd 2022;42(4):1891–908.
[129] Qureshi MZA, et al. Physical impact of nano-layer on nano-fluid flow due to dispersion of magnetized carbon nano-materials through an absorbent channel with thermal analysis. J Mol Liq 2021;325:115211.
[130] Ibrahim M, et al. Study of capabilities of the ANN and RSM models to predict the thermal conductivity of nanofluids containing SiO_2 nanoparticles. J Therm Anal Calorim 2021;145:1993–2003.
[131] Chu YM, et al. Influence of wavy enclosure and nanoparticles on heat release rate of PCM considering numerical study. J Mol Liq 2020;319:114121.
[132] Wang T, et al. Approaches for expedition of discharging of PCM involving nanoparticles and radial fins. J Mol Liq 2021;329:115052.
[133] Naveenraj S, et al. A general microwave synthesis of metal (Ni, Cu, Zn) selenide nanoparticles and their competitive interaction with human serum albumin. New J Chem 2018;42(8):5759–66.
[134] Alahdal M, et al. Trace elements-based Auroshell gold@ hematite nanostructure: green synthesis and their hyperthermia therapy. IET Nanobiotechnol 2023;17(1):22–31.
[135] Ibrahim M, et al. An investigation of the exergy and first and second laws by two-phase numerical simulation of various nanopowders with different diameter on the performance of zigzag-wall micro-heat sink (ZZW-MHS). J Therm Anal Calorim 2021;145(3):1611–21.
[136] Chu YM, et al. Investigation of nano powders influence on melting process within a storage unit. J Mol Liq 2020;318:114321.
[137] Isacfranklin M, et al. Synthesis of highly active biocompatible ZrO_2 nanorods using a bioextract. Ceram Int 2020;46(16):25915–20.
[138] Isacfranklin M, et al. Y_2O_3 nanorods for cytotoxicity evaluation. Ceram Int 2020;46(12):20553–7.
[139] Chu YM, et al. Irregular topological indices of certain metal organic frameworks. Main Group Met Chem 2021;44(1):73–81.
[140] Manzoor S, et al. On topological aspects of degree based entropy for two carbon nanosheets. Main Group Met Chem 2020;43(1):205–18.
[141] Vidhya MS, et al. Anti-cancer applications of Zr, Co, Ni-doped ZnO thin nanoplates. Mater Lett 2021;283:128760.
[142] Kumar V, et al. Analysis of single and multi-wall carbon nanotubes (SWCNT/MWCNT) in the flow of Maxwell nanofluid with the impact of magnetic dipole. Comput Theor Chem 2021;1200:113223.
[143] Chu YM, et al. Examining rheological behavior of MWCNT-TiO_2/5W40 hybrid nanofluid based on experiments and RSM/ANN modeling. J Mol Liq 2021;333:115969.
[144] Maouedj R, et al. Simulating the turbulent hydrothermal behavior of oil/MWCNT nano fluid in a solar channel heat exchanger equipped with vortex generators. Comput Model Eng Sci 2021;126(3):855–89.
[145] Chu YM, et al. On ve-degree and ev-degree based topological properties of H-naphtalenic nanotube. Polycycl Aromat Compd 2022;42(5):2420–32.
[146] Gangu KK, et al. A review on contemporary metal–organic framework materials. Inorg Chim Acta 2016;446:61–74.
[147] Furukawa H, et al. The chemistry and applications of metal-organic frameworks. Science 2013;341(6149):1230444.
[148] Yaghi OM, et al. Reticular synthesis and the design of new materials. Nature 2003;423(6941):705–14.
[149] Kumar P, Paul A, Deep A. Sensitive chemosensing of nitro group containing organophosphate pesticides with MOF-5. Microporous Mesoporous Mater 2014;195:60–6.
[150] Hu C, et al. Toughening mechanisms of epoxy resin using aminated metal-organic framework as additive. Mater Lett 2019;240:113–16.
[151] Xing XS, et al. High proton conduction in an excellent water-stable gadolinium metal–organic framework. Chem Commun 2019;55(9):1241–4.
[152] Mirkovic I, et al. Crystal growth of metal–organic framework-5 around cellulose-based fibers having a necklace morphology. ACS Omega 2019;4(1):169–75.
[153] Yang H, et al. Metal–organic framework coated titanium dioxide nanorod array p–n heterojunction photoanode for solar water-splitting. Nano Res 2019;12(3):643–50.
[154] Meng J, et al. Advances in metal–organic framework coatings: versatile synthesis and broad applications. Chem Soc Rev 2020;49(10):3142–86.
[155] Yang P, et al. Polyoxometalate–cyclodextrin metal–organic frameworks: from tunable structure to customized storage functionality. J Am Chem Soc 2019;141(5):1847–51.
[156] Li Q, et al. An amino-functionalized metal–organic framework nanosheet array as a battery-type electrode for an advanced supercapattery. Dalton Trans 2019;48(46):17163–8.
[157] Liu CY, et al. Ultrafast luminescent light-up guest detection based on the lock of the host molecular vibration. J Am Chem Soc 2020;142(14):6690–7.
[158] Howlader P, Mukherjee PS. Solvent directed synthesis of molecular cage and metal organic framework of copper (II) paddlewheel cluster. Isr J Chem 2019;59(3–4):292–8.
[159] Liu D, Lang JP, Abrahams BF. Highly efficient separation of a solid mixture of naphthalene and anthracene by a reusable porous metal–organic framework through a single-crystal-to-single-crystal transformation. J Am Chem Soc 2011;133(29):11042–5.
[160] Huang X, et al. Fabrication of novel electrochemical sensor based on bimetallic Ce-Ni-MOF for sensitive detection of bisphenol A. Anal Bioanal Chem 2020;412(4):849–60.
[161] Goncalves JM, et al. Recent trends and perspectives in electrochemical sensors based on MOF-derived materials. J Mater Chem C 2021;9(28):8718–45.
[162] Lang JP, et al. $\{[WS_4Cu_4$ (4, 4′-bpy) $_4][WS_4Cu_4I_4$ (4, 4′-bpy) 2]}∞-an unusual 3D porous coordination polymer formed from the preformed cluster $[Et_4N]_4$ $[WS_4Cu_4I_6]$. Angew Chem Int Ed 2004;43(36):4741–5.
[163] Karimian N, et al. A novel sensing layer based on metal–organic framework UiO-66 modified with TiO_2–graphene oxide: application to rapid, sensitive and simultaneous determination of paraoxon and chlorpyrifos. New J Chem 2019;43(6):2600–9.
[164] Bhardwaj R, et al. Layered construction of nano immuno-hybrid embedded MOF as an electrochemical sensor for rapid quantification of total pesticides load in vegetable extract. J Electroanal Chem 2020;873:114386.
[165] AlNadhari S, et al. A review on biogenic synthesis of metal nanoparticles using marine algae and its applications. Environ Res 2021;194:110672.
[166] Bag PP, et al. Synthesis of metal-organic frameworks (MOFs) and their biological, catalytic and energetic application: a mini review. Eng Sci 2020;13(2):1–10.
[167] Oveisi M, Asli MA, Mahmoodi NM. Carbon nanotube based metal-organic framework nanocomposites: synthesis and their photocatalytic activity for decolorization of colored wastewater. Inorg Chim Acta 2019;487:169–76.
[168] Al Sharabati M, Sabouni R, Husseini GA. Biomedical applications of metal– organic frameworks for disease diagnosis and drug delivery: a review. Nanomaterials 2022;12(2):277.
[169] Abazari R, Mahjoub AR, Shariati J. Synthesis of a nanostructured pillar MOF with high adsorption capacity towards antibiotics pollutants from aqueous solution. J Hazard Mater 2019;366:439–51.
[170] Xia SB, et al. Robust hexagonal nut-shaped titanium (IV) MOF with porous structure for ultra-high performance lithium storage. Electrochim Acta 2019;296:746–54.
[171] Shi D, et al. A novel photosensitizing decatungstate-based MOF: synthesis and photocatalytic oxidation of cyclohexane with molecular oxygen. Inorg Chem Commun 2019;100:125–8.
[172] Shinde SK, et al. MOFs-graphene composites synthesis and application for electrochemical supercapacitor: a review. Polymers 2022;14(3):511.
[173] Patel U, et al. The synthesis and characterization of Zn (II)/Cd (II) based MOFs by a mixed ligand strategy: a Zn (II) MOF as a dual functional material for reversible dye adsorption and as a heterogeneous catalyst for the Biginelli reaction. Mater Chem Front 2021;5(1):304–14.
[174] Siva V, et al. Structural, thermal and electro-optical properties of guanidine based Metal-Organic Framework (MOF). Chin J Phys 2020;68:764–77.
[175] Dhivya E, et al. Synthesis of titanium based hetero MOF photocatalyst for reduction of Cr (VI) from wastewater. J Environ Chem Eng 2019;7(4):103240.
[176] Wei JZ, et al. Rapid and low-cost electrochemical synthesis of UiO-66-NH_2 with enhanced fluorescence detection performance. Inorg Chem 2019;58(10):6742–7.
[177] Lu C, et al. Electrochemical synthesis of a microporous conductive polymer based on a metal–organic framework thin film. Angew Chem Int Ed 2014;126(25):6572–6.
[178] Zhou S, et al. Paralyzed membrane: current-driven synthesis of a metal-organic framework with sharpened propene/propane separation. Sci Adv 2018;4(10):eaau1393.
[179] Asghar A, et al. Efficient electrochemical synthesis of a manganese-based metal–organic framework for H_2 and CO_2 uptake. Green Chem 2021;23(3):1220–7.
[180] Simon-Yarza T, et al. Nanoparticles of metal-organic frameworks: on the road to *in vivo* efficacy in biomedicine. Adv Mater 2018;30(37):1707365.
[181] Chen W, Du L, Wu C. Hydrothermal synthesis of MOFs, in metal-organic frameworks for biomedical applications. Elsevier; 2020. p. 141–57.
[182] Chen W, Wu C. Synthesis, functionalization, and applications of metal–organic frameworks in biomedicine. Dalton Trans 2018;47(7):2114–33.
[183] Liu W, et al. Mg-MOF-74/MgF2 composite coating for improving the properties of magnesium alloy implants: hydrophilicity and corrosion resistance. Materials 2018;11(3):396.
[184] Cheng W, et al. One-step microwave hydrothermal preparation of Cd/Zr-bimetallic metal–organic frameworks for enhanced photochemical properties. Adv Compos Hybrid Mater 2021;4(1):150–61.
[185] Vaitsis C, Sourkouni G, Argirusis C. Metal organic frameworks (MOFs) and ultrasound: a review. Ultrason Sonochem 2019;52:106–19.
[186] Ramezanzadeh M, Ramezanzadeh B. Thermomechanical and anticorrosion characteristics of metal-organic frameworks. In: Metal-organic frameworks for chemical reactions. Elsevier; 2021. p. 295–330.
[187] Jiang L, et al. Recent advances of metal–organic frameworks in corrosion protection: from synthesis to applications. Chem Eng J 2022;430:132823.

[188] Yu K, et al. Sonochemical synthesis of Zr-based porphyrinic MOF-525 and MOF-545: enhancement in catalytic and adsorption properties. Microporous Mesoporous Mater 2021;316:110985.
[189] Tanhaei M, Mahjoub AR, Safarifard V. Energy-efficient sonochemical approach for the preparation of nanohybrid composites from graphene oxide and metal-organic framework. Inorg Chem Commun 2019;102:185–91.
[190] Zhou Q, et al. Magnetic solid phase extraction of N-and S-containing polycyclic aromatic hydrocarbons at ppb levels by using a zerovalent iron nanoscale material modified with a metal organic framework of type Fe@ MOF-5, and their determination by HPLC. Microchim Acta 2017;184(4):1029–36.
[191] Zheng J, et al. Mechanism of CeO_2 synthesized by thermal decomposition of Ce-MOF and its performance of benzene catalytic combustion. J Rare Earths 2021;39(7):790–6.
[192] Iqbal B, Laybourn A, Zaheer M. Size-controlled synthesis of spinel nickel ferrite nanorods by thermal decomposition of a bimetallic Fe/Ni-MOF. Ceram Int 2021;47(9):12433–41.
[193] Kim DY, et al. Green synthesis of silver nanoparticles using Laminaria japonica extract: characterization and seedling growth assessment. J Clean Prod 2018;172:2910–18.
[194] Alduhaish OM, Shaik MR, Adil SF. Photo-induced preparation of Ag@ MOF-801 composite based heterogeneous nanocatalyst for the production of biodiesel. Catalysts 2022;12(5):533.
[195] Gaikwad S, et al. Controllable synthesis of 1, 3, 5-tris (1H-benzo [d] imidazole-2-yl) benzene-based MOFs. Appl Sci 2021;11(21):9856.
[196] Vaidya LB, Nadar SS, Rathod VK. Biological metal organic framework (bio-MOF) of glucoamylase with enhanced stability. Colloids Surf B 2020;193:111052.
[197] Makuve N, et al. Hydrogenation of carbon dioxide to Formate using a cadmium-based metal–organic framework impregnated with nanoparticles. Inorganics 2022;10(3):30.
[198] Rabiee Faradonbeh M, et al. Newly MOF-graphene hybrid nanoadsorbent for removal of Ni (II) from aqueous phase. J Inorg Organomet Polym Mater 2018;28(3):829–36.
[199] Nguyen Thi HT, et al. Enhanced degradation of Rhodamine B by metallic organic frameworks based on NH2-MIL-125 (Ti) under visible light. Materials 2021;14(24):7741.
[200] Mehmandoust MR, Motakef-Kazemi N, Ashouri F. Nitrate adsorption from aqueous solution by metal–organic framework MOF-5. Iran J Sci Technol Trans Sci 2019;43(2):443–9.
[201] Shaik MR, et al. Fumarate based metal–organic framework: an effective catalyst for the transesterification of used vegetable oil. Crystals 2022;12(2):151.
[202] Jagan Mohan Reddy A, et al. Fabrication and deployment of nanodisc ZnO@ ZIF-8, ZnO@ NA and ZnO@ INA core–shell MOFs: enhanced NH3 and HCHO gas sensing. J Mater Sci: Mater Electron 2021;32(6):7827–40.
[203] Shen J, et al. Efficient adsorption of Pb (II) from aqueous solutions by metal organic framework (Zn-BDC) coated magnetic montmorillonite. Polymers 2018;10(12):1383.
[204] Liu C, et al. Ternary MOF-on-MOF heterostructures with controllable architectural and compositional complexity via multiple selective assembly. Nat Commun 2020;11(1):1–8.
[205] Hassan MH, Khan R, Andreescu S. Advances in electrochemical detection methods for measuring contaminants of emerging concerns. Electrochem Sci Adv 2022;2(6):e2100184.
[206] Gorbova E, et al. Fundamentals and principles of solid-state electrochemical sensors for high temperature gas detection. Catalysts 2022;12(1):1.
[207] Anupriya J, et al. Raspberry-like $CuWO_4$ hollow spheres anchored on sulfur-doped g-C_3N_4 composite: an efficient electrocatalyst for selective electrochemical detection of antibiotic drug nitrofurazone. Chemosphere 2022;296:133997.
[208] Yin M, et al. Detection of antibiotics by electrochemical sensors based on metal-organic frameworks and their derived materials. Microchem J 2022;183:107946.
[209] Gupta VK, et al. Voltammetric techniques for the assay of pharmaceuticals-a review. Anal Biochem 2011;408(2):179.
[210] Chen C, et al. Preparation and application of nitrofuran sensor in aquaculture water. Int J Environ Anal Chem 2021;101(8):1099–115.
[211] Cheng J, et al. Molecularly imprinted electrochemical sensor based on biomass carbon decorated with MOF-derived Cr_2O_3 and silver nanoparticles for selective and sensitive detection of nitrofurazone. Chem Eng J 2020;398:125664.
[212] Zhang D, et al. Copper cobalt sulfide structures derived from MOF precursors with enhanced electrochemical glucose sensing properties. Nanomaterials 2022;12(9):1394.
[213] Naghian E, et al. A new electrochemical sensor for the detection of fentanyl lethal drug by a screen-printed carbon electrode modified with the open-ended channels of Zn (ii)-MOF. New J Chem 2020;44(22):9271–7.
[214] Alsafrani AE, et al. Efficient synthesis and characterization of polyaniline@ aluminium–succinate metal-organic frameworks nanocomposite and its application for Zn (II) ion sensing. Polymers 2021;13(19):3383.
[215] Yang M, et al. Sulfur nanoparticle-encapsulated MOF and boron nanosheet–ferrocene complex modified electrode platform for ratiometric electrochemical sensing of adriamycin and real-time monitoring of drug release. Microchem J 2022;177:107319.
[216] Xiong C, et al. Synthesis and characterization of Ru-MOFs on microelectrode for trace mercury detection. Sensors 2020;20(22):6686.
[217] Ling Y, et al. Immunoaffinity-induced signal depression of Cu-MOF-74 for label-free electrochemical detection of cardiac troponin I. J Phys Chem C 2022;;126:9416–24.
[218] Lv R, et al. Cu^{2+} modified Zr-based metal organic framework-CTAB-graphene for sensitive electrochemical detection of sunset yellow. Food Chem Toxicol 2022;166:113250.
[219] Prasanna SB, et al. MOF derived 2D-flake-like structured $Mn_3Co_3O_4$ integrated acid functionalized MWCNT for electrochemical detection of antibiotic furazolidone in biological fluids. Appl Surf Sci 2023;611:155784.
[220] Zhang X, et al. Homocysteine inhibits pro-insulin receptor cleavage and causes insulin resistance via protein cysteine-homocysteinylation. Cell Rep 2021;37(2):109821.
[221] Ameen F, et al. Antioxidant, antibacterial and anticancer efficacy of Alternaria chlamydospora-mediated gold nanoparticles. Appl Nanosci 2022;13:2233–40.
[222] Khan A, et al. Fabrication and antibacterial activity of nanoenhanced conjugate of silver (I) oxide with graphene oxide. Mater Today Commun 2020;25:101667.
[223] Ameen F, et al. Fabrication of silver nanoparticles employing the cyanobacterium Spirulina platensis and its bactericidal effect against opportunistic nosocomial pathogens of the respiratory tract. J Mol Struct 2020;1217:128392.
[224] Gangalla R, et al. Optimization and characterization of exopolysaccharide produced by Bacillus aerophilus rk1 and its *in vitro* antioxidant activities. J King Saud Univ Sci 2021;33(5):101470.
[225] Shen M, et al. Antibacterial applications of metal–organic frameworks and their composites. Compr Rev Food Sci Food Saf 2020;19(4):1397–419.
[226] Jo JH, et al. Antibacterial activities of Cu-MOFs containing glutarates and bipyridyl ligands. Dalton Trans 2019;48(23):8084–93.
[227] Almansob A, Bahkali AH, Ameen F. Efficacy of gold nanoparticles against drug-resistant nosocomial fungal pathogens and their extracellular enzymes: resistance profiling towards established antifungal agents. Nanomaterials 2022;12(5):814.
[228] Hu WC, et al. *In situ* fabrication of ultrasmall gold nanoparticles/2D MOFs hybrid as nanozyme for antibacterial therapy. Small 2020;16(23):2000553.
[229] Sarika K, et al. Antimicrobial and antifungal activity of soil actinomycetes isolated from coal mine sites. Saudi J Biol Sci 2021;28(6):3553–8.
[230] Kundu B, Reis RL, Kundu SC. Biomimetic antibacterial pro-osteogenic Cu-Sericin MOFs for osteomyelitis treatment. Biomimetics 2022;7(2):64.
[231] Chen M, et al. Titanium incorporation into Zr-porphyrinic metal–organic frameworks with enhanced antibacterial activity against multidrug-resistant pathogens. Small 2020;16(7):1906240.
[232] Guo W, et al. Plasmon-enhanced visible-light photocatalytic antibacterial activity of metal-organic framework/gold nanocomposites. J Mater Chem A 2023.
[233] Ameen F, et al. Anti-oxidant, anti-fungal and cytotoxic effects of silver nanoparticles synthesized using marine fungus Cladosporium halotolerans. Appl Nanosci 2023;13(1):623–31.
[234] Li J, et al. Preparation of 2D ZIF-L and its antibacterial and antifouling properties. Nanomaterials 2023;13(1):202.
[235] Xie Q, et al. Active edible films with plant extracts: a updated review of their types, preparations, reinforcing properties, and applications in muscle foods packaging and preservation. Crit Rev Food Sci Nutr 2022;1:1–23.
[236] Al-Enazi NM, et al. Tin oxide nanoparticles (SnO_2-NPs) synthesis using Galaxaura elongata and its anti-microbial and cytotoxicity study: a greenery approach. Appl Nanosci 2021;13:519–27.
[237] Feng S, et al. Development of novel Co-MOF loaded sodium alginate based packaging films with antimicrobial and ammonia-sensitive functions for shrimp freshness monitoring. Food Hydrocoll 2023;135:108193.
[238] Mohammed AE, et al. In-silico predicting as a tool to develop plant-based biomedicines and nanoparticles: lycium shawii metabolites. Biomed Pharmacother 2022;150:113008.
[239] Zhang J, et al. NO released via both a Cu-MOF-based donor and surface-catalyzed generation enhances anticoagulation and antibacterial surface effects. Biomater Sci 2023;11(1):322–38.
[240] Ibrahim M, et al. Optimization and effect of wall conduction on natural convection in a cavity with constant temperature heat source: using lattice Boltzmann method and neural network algorithm. J Therm Anal Calorim 2021;144:2449–63.
[241] Chu YM, et al. Topological study of polycyclic graphite carbon nitride. Polycycl Aromat Compd 2022;42(6):3203–15.
[242] Chu YM, Siddiqui MK, Nasir M. On topological co-indices of polycyclic tetrathiafulvalene and polycyclic oragano silicon dendrimers. Polycycl Aromat Compd 2022;42(5):2179–97.
[243] Muhammad MH, et al. On topological analysis of graphite carbon nitride via degree based coindices. Polycycl Aromat Compd 2022;42(5):2777–88.
[244] Chu YM, et al. Computation of zagreb polynomials and zagreb indices for benzenoid triangular & hourglass system. Polycycl Aromat Compd 2022:1–10.
[245] Siddiqui MK, et al. On analysis of thermodynamic properties of cuboctahedral bi-metallic structure. Main Group Met Chem 2021;44(1):117–28.
[246] Nazeer M, et al. Mathematical modeling of multiphase flows of third-grade fluid with lubrication effects through an inclined channel: analytical treatment. J Dispers Sci Technol 2022;43(10):1555–67.
[247] Iqbal A, et al. Hermite-Hadamard type inequalities pertaining conformable fractional integrals and their applications. AIP Adv 2018;8(7):075101.
[248] Chu Y, Khater MM, Hamed Y. Diverse novel analytical and semi-analytical wave solutions of the generalized (2+ 1)-dimensional shallow water waves model. AIP Adv 2021;11(1):015223.
[249] Nazeer M, et al. Perturbation solution of the multiphase flows of third grade dispersions suspended with Hafnium and crystal particles. Surf Interfaces 2021;22:100803.
[250] Khan D, et al. A new idea of fractal-fractional derivative with power law kernel for free convection heat transfer in a channel flow between two static upright parallel plates. Comput Mater Contin 2020;65(2): 1237–1251.
[251] Chu Y, et al. Computer methodologies for the comparison of some efficient derivative free simultaneous iterative methods for finding roots of non-linear equations. Comput Mater Contin 2020;66(1):275–90.

[252] Ullah Z, et al. Computational analysis of the oscillatory mixed convection flow along a horizontal circular cylinder in thermally stratified medium. CMC Comput Mater Contin 2020;65(1):109–23.
[253] Cui G, et al. Adaptive decentralized NN control of large-scale stochastic nonlinear time-delay systems with unknown dead-zone inputs. Neurocomputing 2015;158:194–203.
[254] Tan F, et al. Fixed-time stochastic outer synchronization in double-layered multi--weighted coupling networks with adaptive chattering-free control. Neurocomputing 2020;399:8–17.
[255] Chen J, et al. New relaxed stability and stabilization conditions for continuous-time T–S fuzzy models. Inf Sci 2016;329:447–60.
[256] Rashid S, et al. New computation of unified bounds via a more general fractional operator using generalized Mittag–Leffler function in the kernel. Comput Model Eng Sci 2021;126(1):359–78.
[257] Riaz M, et al. A robust q-rung orthopair fuzzy Einstein prioritized aggregation operators with application towards MCGDM. Symmetry 2020;12(6):1058.
[258] Kumar S, et al. An optimal fourth order derivative-free numerical algorithm for multiple roots. Symmetry 2020;12(6):1038.
[259] Kalsoom H, et al. Two-variable quantum integral inequalities of Simpson-type based on higher-order generalized strongly preinvex and quasi-preinvex functions. Symmetry 2019;12(1):51.
[260] Rashid S, et al. New multi-parametrized estimates having pth-order differentiability in fractional calculus for predominating $\hbar$-convex functions in Hilbert space. Symmetry 2020;12(2):222.
[261] Rashid S, et al. Fractional integral inequalities for strongly h-preinvex functions for ak th order differentiable functions. Symmetry 2019;11(12):1448.
[262] Munir M, et al. T-spherical fuzzy Einstein hybrid aggregation operators and their applications in multi-attribute decision making problems. Symmetry 2020;12(3):365.
[263] Chu HH, et al. Quantum analogs of Ostrowski-type inequalities for raina's function correlated with coordinated generalized Φ-convex functions. Symmetry 2020;12(2):308.
[264] Wang Y, et al. Asynchronous finite-time state estimation for semi-Markovian jump neural networks with randomly occurred sensor nonlinearities. Neurocomputing 2021;432:240–9.
[265] Kadkhoda N, et al. New exact solutions and conservation laws to the fractional-order Fokker–Planck equations. Symmetry 2020;12(8):1282.
[266] Riaz M, et al. Spherical linear diophantine fuzzy sets with modeling uncertainties in MCDM. Comput Model Eng Sci 2021;126(3):1125–64.
[267] Liu L, et al. The applications of metal– organic frameworks in electrochemical sensors. ChemElectroChem 2018;5(1):6–19.
[268] Peng Y, et al. Hybridization of MOFs and COFs: a new strategy for construction of MOF@ COF core–shell hybrid materials. Adv Mater 2018;30(3):1705454.
[269] Hong Y, et al. 3D printed microfluidic device with microporous Mn_2O_3-modified screen printed electrode for real-time determination of heavy metal ions. ACS Appl Mater Interfaces 2016;8(48):32940–7.
[270] Liu CS, Li J, Pang H. Metal-organic framework-based materials as an emerging platform for advanced electrochemical sensing. Coord Chem Rev 2020;410:213222.
[271] Begum I, et al. Facile fabrication of malonic acid capped silver nanoparticles and their antibacterial activity. J King Saud Univ Sci 2021;33(1):101231.